Computer Methods in Applied Mechanics and Engineering 435 (2025) 117485

Contents lists available at ScienceDirect

Comput. Methods Appl. Mech. Engrg.

journal homepage: www.elsevier.com/locate/cma

A software benchmark for cardiac elastodynamics

Reidmen Aróstica [a,1], David Nolte [a,1], Aaron Brown [j,l], Amadeus Gebauer [b,1], Elias Karabelas [o,p,1], Javiera Jilberto [m,1], Matteo Salvador [e,k,l], Michele Bucelli [e], Roberto Piersanti [e,1], Kasra Osouli [d,1], Christoph Augustin [f,1], Henrik Finsberg [c,1], Lei Shi [i,n,1], Marc Hirschvogel [e,g,1], Martin Pfaller [j], Pasquale Claudio Africa [e,h,1], Matthias Gsell [f], Alison Marsden [j,k,l], David Nordsletten [g,m], Francesco Regazzoni [e], Gernot Plank [f], Joakim Sundnes [c], Luca Dede' [e], Mathias Peirlinck [d,1], Vijay Vedula [i,1], Wolfgang Wall [b], Cristóbal Bertoglio [a,*]

[a] Bernoulli Institute, University of Groningen, Groningen, The Netherlands
[b] Institute for Computational Mechanics, Technische Universität München, Garching, Germany
[c] Simula Research Laboratory, Oslo, Norway
[d] Department of Biomechanical Engineering, Delft University of Technology, Delft, The Netherlands
[e] Modellistica e Calcolo Scientifico (MOX), Dipartimento di Matematica, Politecnico di Milano, Milan, Italy
[f] Gottfried Schatz Research Center: Division of Biophysics, Medical University of Graz, Graz, Austria
[g] Division of Biomedical Engineering and Imaging Sciences, Department of Biomedical Engineering, King's College London, London, UK
[h] SISSA, International School for Advanced Studies, Trieste, Italy
[i] Department of Mechanical Engineering, Columbia University, New York, NY, USA
[j] Department of Mechanical Engineering, Stanford University, Stanford, CA, USA
[k] Institute for Computational and Mathematical Engineering, Stanford University, Stanford, CA, USA
[l] Stanford Cardiovascular Institute, Stanford, CA, USA
[m] Department of Biomedical Engineering, University of Michigan, Ann Arbor, USA
[n] Department of Mechanical Engineering, Kennesaw State University, Marietta, GA, USA
[o] Department of Mathematics & Scientific Computing, NAWI Graz, University of Graz, Graz, Austria
[p] BioTechMed-Graz, Graz, Austria

ARTICLE INFO

Keywords:
Cardiac mechanics
Software
Finite elements
Benchmark
Hyperelasticity

ABSTRACT

In cardiovascular mechanics, reaching consensus in simulation results within a physiologically relevant range of parameters is essential for reproducibility purposes. Although currently available benchmarks contain some of the features that cardiac mechanics models typically include, some important modeling aspects are missing. Therefore, we propose a new set of cardiac benchmark problems and solutions for assessing passive and active material behavior, viscous effects, and pericardial boundary condition. The problems proposed include simplified analytical fiber definitions and active stress models on a monoventricular and biventricular domains, allowing straightforward testing and validation with already developed solvers.

* Corresponding author.
E-mail address: c.a.bertoglio@rug.nl (C. Bertoglio).
[1] First authors.

https://doi.org/10.1016/j.cma.2024.117485
Received 27 May 2024; Received in revised form 9 October 2024; Accepted 18 October 2024
Available online 19 December 2024

1. Introduction

In computational biomechanics in general, efforts of defining benchmarks for verification and validation have been sparse throughout the years and are application dependent [1–4].

In particular, in the context of cardiovascular mechanics, reaching consensus in simulation results is an important task, since, for a given set of physical constants, different numerical solutions can be obtained, e.g., due to discretization strategies, polynomial degree of basis functions, numerical quadratures and time integrators [5–14]. Specially, when parameters are optimized from clinical data, it is crucial that these parameters may be valid for other groups and hence could be reused, given the high complexity involved in solving these inverse problems [15–17]

In [2] was proposed a first benchmark containing some of the features that cardiac mechanics models typically include. However some important features are lacking, such as the inclusion of state-of-the-art passive and active models, idealized geometrical dimensions, boundary conditions as well as time dependent effects (i.e. inertia and viscosity).

Therefore, we propose here a new set of cardiac benchmark problems and computed solutions for assessing passive and active material behavior as in [18] with viscous effects and pericardial boundary conditions as in [7]. The problems proposed in this work include a simplified analytical fiber definition with active stress model by [19], allowing straightforward testing and validation with already developed solvers. The benchmark definition is agreed upon nine different research groups, who computed their solutions with numerical methods and software of their choice. A comparison is carried out among the solutions computed by the different groups, whose results demonstrate a substantial agreement between the participating teams.

The remainder of this article is organized as follows. Section 2 describes the mechanical problem in continuous form, its material properties and boundary conditions. Section 3 proposes the first benchmark problem in a monoventricular domain, with analytical geometry, fibers orientation and simulations setup for blinded and non-blinded phases among participants. Section 4 proposes a second benchmark for a biventricular domain, with state-of-the-art fiber orientation, constitutive law and analogous setups to Section 3 comprising a non-blinded phase only. Section 5 describes all participant software as well as their solver strategies. Section 6 contains computed results with a qualitative and quantitative analysis of the first and second benchmark. Section 7 provides a discussion of the different approaches and results, finally in Section 9 the conclusion.

2. The mathematical model

2.1. Strong form

We define the problem in a domain $\Omega \subset \mathbb{R}^3$ with boundary $\partial\Omega := \Gamma_{top} \cup \Gamma_{epi} \cup \Gamma_{endo}$. Let us denote by $\mathbf{u} : \Omega \to \mathbb{R}^3$ the displacement field to be found, $\mathbf{u}(\mathbf{X})$ its evaluation in $\mathbf{X}$ for $\mathbf{X} \in \Omega$, by $\mathbb{F} := \mathbb{I} + \mathbf{Grad}(\mathbf{u}) := \mathbb{I} + \frac{\partial \mathbf{u}}{\partial \mathbf{X}}$ the deformation gradient, $\mathbf{Div}(\mathbf{u}) := \frac{\partial}{\partial \mathbf{X}} \cdot \mathbf{u}$ the divergence, $J := \det(\mathbb{F}(\mathbf{u})) := \det(\mathbb{F})$ the jacobian, $\mathbb{E} = \frac{1}{2}(\mathbb{C} - \mathbb{I})$ the Green–Lagrange tensor, $\mathbb{C} := \mathbb{F}^\top\mathbb{F}$ the right Cauchy tensor and $\mathbb{I}$ and the identity matrix respectively.

Let us denote $\mathbb{T} := \mathbb{T}(\mathbf{u})$ the Cauchy stress tensor associated to the unknown displacement field $\mathbf{u}$ and the second Piola Kirchhoff stress tensor denoted by $\mathbb{S} := J\mathbb{F}^{-1}\mathbb{T}\mathbb{F}^{-\top}$, the problem to solve over the time-interval $(0, 1]$, is described by the equations:

$$\begin{aligned}
\rho\ddot{\mathbf{u}} - \mathbf{Div}\left(J\mathbb{T}\mathbb{F}^{-\top}\right) = \mathbf{0} \quad & \text{in } \Omega \\
J\mathbb{T}\mathbb{F}^{-\top}\mathbf{N} = pJ\mathbb{F}^{-\top}\mathbf{N} \quad & \text{on } \Gamma_{endo} \\
J\mathbb{T}\mathbb{F}^{-\top}\mathbf{N}\cdot\mathbf{N} + \alpha_{epi}\mathbf{u}\cdot\mathbf{N} + \beta_{epi}\dot{\mathbf{u}}\cdot\mathbf{N} = 0 \quad & \text{on } \Gamma_{epi} \\
J\mathbb{T}(\mathbb{F}^{-\top}\mathbf{N}) \times \mathbf{N} = \mathbf{0} \quad & \text{on } \Gamma_{epi} \\
J\mathbb{T}\mathbb{F}^{-\top}\mathbf{N} + \alpha_{top}\mathbf{u} + \beta_{top}\dot{\mathbf{u}} = \mathbf{0} \quad & \text{on } \Gamma_{top}
\end{aligned} \tag{1}$$

with $\mathbf{N}$ the unit wall normal vector and $\top$ the transpose if used as superscript.

2.2. Material model

The material behavior is characterized via $\mathbb{S}$ including the anisotropic, viscous and active parts, namely

$$\mathbb{S}(t) := \frac{\partial \Psi_{aniso}}{\partial \mathbb{E}} + \frac{\partial \Psi_{visco}}{\partial \dot{\mathbb{E}}} + \tau(t)\mathbf{f} \otimes \mathbf{f}, \tag{2}$$

with each term described below[2]:

[2] Models aiming at characterizing the strain–stress behavior have been substantially studied [18,20–22]. The literature points at the work of *Guccione* et al. [23] and *Holzapfel* et al. [18], the latter widely used for human cardiac models. Nevertheless, not only one convention has been used to characterize the fiber orientation, especially with the choice of the sheet and sheet-normal directions. Several works implementing either case have shown consistent deformations, endocardial pressure as well as ejection volumes [6,24–30].

- The anisotropic material energy Ψ_{aniso} describes the nearly incompressible Holzapfel–Ogden material [18] with isochoric-volumetric split, via the isotropic invariant $I_1 = J^{-2/3}\mathrm{tr}(\mathbb{C})$, the transverse isotropic invariants $I_{4f} := \mathbf{f}\cdot\mathbb{C}\mathbf{f}$ and $I_{4s} := \mathbf{s}\cdot\mathbb{C}\mathbf{s}$ for the fiber directions at the reference domain $\mathbf{f},\mathbf{s} : \Omega \to \mathbb{R}^3$ and anisotropic invariant $I_{8fs} := \mathbf{f}\cdot\mathbb{C}\mathbf{s}$. Explicitly Ψ_{aniso} is given by:

$$\begin{aligned}\Psi_{aniso} = \frac{a}{2b}\exp\big\{b(I_1-3)\big\} + \sum_{i\in\{f,s\}}\frac{a_i}{2b_i}\chi(I_{4i})\big(\exp\big\{b_i(I_{4i}-1)^2\big\}-1\big)\\ + \frac{a_{fs}}{2b_{fs}}\big(\exp\{b_{fs}I_{8fs}^2\}-1\big) + \frac{\kappa}{4}\big(J^2-1-2\ln(J)\big)\end{aligned} \tag{3}$$

  with $\chi(x) = x$ if $x > 1$ and 0 elsewise, for $x \in \mathbb{R}_+$, denoting the fiber compression switch model. The last term denotes the incompressibility penalty proposed in [31] with parameter $\kappa > 0$.
  A suggested approximation is given by $\chi(x) \approx \frac{1}{1+e^{-k(x-1)}}$, for $k > 0$ a fixed parameter specified later on.
- The viscoelastic energy is characterized with parameter η in the form [32]:

$$\Psi_{visc} := \frac{\eta}{2}\mathrm{tr}(\dot{\mathbb{E}}^2) \tag{4}$$

- The active stress is taken as in [19], characterized by a time-dependent stress function τ, solution to the evolution equation

$$\dot{\tau}(t) = -|a(t)|\tau(t) + \sigma_0|a(t)|_+ \tag{5}$$

  denoting $a(\cdot)$ the activation function and σ_0 contractility, and the remaining terms defined as:

$$\begin{aligned}|a(t)|_+ &= \max\{a(t),0\}\\ a(t) &:= \alpha_{max}\cdot f(t) + \alpha_{min}\cdot(1-f(t))\\ f(t) &= S^+(t-t_{sys})\cdot S^-(t-t_{dias})\\ S^\pm(\Delta t) &= \frac{1}{2}\big(1\pm\tanh(\frac{\Delta t}{\gamma})\big).\end{aligned} \tag{6}$$

2.3. Pressure model

We consider a time-dependent pressure for (1), derived from the active stress function. The solution $p = p(t)$ is characterized by the evolution equation

$$\dot{p}(t) = -|b(t)|p(t) + \sigma_{mid}|b(t)|_+ + \sigma_{pre}|g_{pre}(t)|_+ \tag{7}$$

with $b(\cdot)$ the activation function described as:

$$\begin{aligned}b(t) &= a_{pre}(t) + \alpha_{pre}g_{pre}(t) + \alpha_{mid}\\ a_{pre}(t) &:= \alpha_{max}\cdot f_{pre}(t) + \alpha_{min}\cdot(1-f_{pre}(t))\\ f_{pre}(t) &= S^+(t-t_{sys-pre})\cdot S^-(t-t_{dias-pre})\\ g_{pre}(t) &= S^-(t-t_{dias-pre})\end{aligned} \tag{8}$$

and $S^\pm$ defined as in (6).

3. Benchmark 1: monoventricular mechanics

3.1. Geometry

Using the same analytical formula as in [2], we define the domain via the parametrization (in $\mathbb{R}^3$) for a truncated ellipsoid, i.e., satisfying:

$$(x,y,z) = \big(r_{\text{long}}\cos(\mu), r_{\text{short}}\sin(\mu)\cos(\theta), r_{\text{short}}\sin(\mu)\sin(\theta)\big) \tag{9}$$

with the following dimensions:

- The endocardial surface

$$r_{\text{short}} = 2.5\times10^{-2}\,[\text{m}],\quad r_{\text{long}} = 9.0\times10^{-2}\,[\text{m}],\quad \mu\in[-\pi,-\arccos(\frac{5}{17})],\theta\in[-\pi,\pi] \tag{10}$$

- The epicardial surface

$$r_{\text{short}} = 3.5\times10^{-2}\,[\text{m}],\quad r_{\text{long}} = 9.7\times10^{-2}\,[\text{m}],\quad \mu\in[-\pi,-\arccos(\frac{5}{20})],\theta\in[-\pi,\pi] \tag{11}$$

The domain is created using the software *Gmsh* [33] and distributed to all participants in different formats, created with an element size[3] $h = 5 \times 10^{-3}$ [m]. Supplemented material is provided with such data as well as a repository including implementation details.[4]

3.2. Fibers

The definition of fibers is based on a local coordinate system derived from the ellipsoid parametrization. Using the ellipsoid parametrization, a point $\mathbf{x}$ in the domain Ω is described as:

$$\mathbf{x}(\mu, \theta, \bar{t}) = \left(r_l(\bar{t})\cos(\mu), r_s(\bar{t})\sin(\mu)\cos(\theta), r_s(\bar{t})\sin(\mu)\sin(\theta)\right), \tag{12}$$

with μ, θ as defined previously and $\bar{t} : \Omega \to [0, 1]$ is defined as the solution to the problem:

$$\begin{aligned} \Delta\bar{t} &= 0 \quad \text{in } \Omega \\ \bar{t} &= 0 \quad \text{on } \Gamma_{endo} \\ \bar{t} &= 1 \quad \text{on } \Gamma_{epi} \\ \frac{\partial\bar{t}}{\partial\mathbf{N}} &= 0 \quad \text{on } \Gamma_{top}. \end{aligned} \tag{13}$$

The tangent basis derived from (12), denoted as $[\mathbf{e}_{\bar{t}}, \mathbf{e}_\mu, \mathbf{e}_\theta]$, is defined as:

$$\begin{aligned} &\tilde{\mathbf{e}}_{\bar{t}} = \frac{\partial\mathbf{x}}{\partial\bar{t}}, \quad \tilde{\mathbf{e}}_\mu = \frac{\partial\mathbf{x}}{\partial\mu}, \quad \tilde{\mathbf{e}}_\theta = \frac{\partial\mathbf{x}}{\partial\theta} \\ &\mathbf{e}_{\bar{t}} = \frac{\tilde{\mathbf{e}}_{\bar{t}}}{\|\tilde{\mathbf{e}}_{\bar{t}}\|_{\mathbb{R}^3}}, \quad \mathbf{e}_\mu = \frac{\tilde{\mathbf{e}}_\mu}{\|\tilde{\mathbf{e}}_\mu\|_{\mathbb{R}^3}}, \quad \mathbf{e}_\theta = \frac{\tilde{\mathbf{e}}_\theta}{\|\tilde{\mathbf{e}}_\theta\|_{\mathbb{R}^3}}, \end{aligned} \tag{14}$$

Using (14), the fiber, sheet-normal and sheet directions are defined as follows:

$$\begin{aligned} \mathbf{f}(\bar{t}, \mu, \theta) &= \sin(\alpha(\bar{t}))\,\mathbf{e}_\mu + \cos(\alpha(\bar{t}))\,\mathbf{e}_\theta \\ \mathbf{n}(\bar{t}, \mu, \theta) &= \frac{\mathbf{e}_\mu \times \mathbf{e}_\theta}{\|\mathbf{e}_\mu \times \mathbf{e}_\theta\|_{\mathbb{R}^3}} \\ \mathbf{s}(\bar{t}, \mu, \theta) &= \frac{\mathbf{f}(\bar{t}, \mu, \theta) \times \mathbf{n}(\bar{t}, \mu, \theta)}{\|\mathbf{f}(\bar{t}, \mu, \theta) \times \mathbf{n}(\bar{t}, \mu, \theta)\|_{\mathbb{R}^3}} \end{aligned} \tag{15}$$

with $\alpha(\bar{t}), r_l(\bar{t}), r_s(\bar{t})$ parameters defined as:

$$\begin{aligned} \alpha(\bar{t}) &= \left(\alpha_{endo} + (\alpha_{epi} - \alpha_{endo})\bar{t}\right)\frac{\pi}{180} \\ r_l(\bar{t}) &= r_{\text{long\_endo}} + (r_{\text{long\_epi}} - r_{\text{long\_endo}})\bar{t} \\ r_s(\bar{t}) &= r_{\text{short\_endo}} + (r_{\text{short\_epi}} - r_{\text{short\_endo}})\bar{t} \end{aligned} \tag{16}$$

for $r_{\text{long\_endo}}, r_{\text{short\_endo}}$ the long/short radius in (10) and $r_{\text{long\_epi}}, r_{\text{short\_epi}}$ the long/short radius in (11).

The computation of the fibers close to the apex is problematic. Given a point in the ellipsoid $\mathbf{x} = (x, y, z)$ and $\bar{t} = \bar{t}(\mathbf{x})$ we propose to compute the associated parameters μ, θ to such a point as $\mu = \operatorname{atan2}(a, b)$ for $a = \frac{\sqrt{y^2+z^2}}{r_s(\bar{t})}, b = \frac{x}{r_l(\bar{t})}$ and $\theta = 0$ if $\mu \leq 10^{-7}$ else $\theta = \pi - \operatorname{atan2}(z, -y)$.

Depicted in Fig. 1 is the labeled ellipsoid geometry, including the fiber and sheet directions.

3.3. Step 0 (non-blinded): Splitting passive and active responses

We first perform a validation with teams having access to the solutions of the rest of participants. This served to refine the problem description and to encourage a larger number of participants.

3.3.1. Case A: Active response

Each group solves numerically the equations described in Section 2, with geometry and fibers as in Sections 3.1 and 3.2 respectively, parameters as in Tables 1, 2, 3 and a zero endocardial pressure, i.e. $p = 0$ on Γ_{endo} over all timesteps.

The groups are requested to provide the displacement field $\mathbf{u}_h(\mathbf{X})$ over time at two spatial locations, $\mathbf{p}_0 = (0.025, 0.03, 0)$, $\mathbf{p}_1 = (0, 0.03, 0)$. Such spatial locations do not describe points of the mesh provided to the participants, thus each team must have interpolation algorithms available.

Depicted in Fig. 2 is the evolution of the stress function τ over time for physical parameters specified therein.

[3] The element size is defined as the optimal edge length around any point node in the mesh with specified target size $h > 0$. Therefore, not a lower or upper edge limit, rather, an averaged value computed to match a user-provided target size. For further details, we refer to [33].

[4] The repository cardiac-benchmark-toolkit stores the data provided to all teams in several formats `.geo`, `.msh`, `.xdmf`, `.h5`, as well as an user-friendly interface to recreate the monoventricular domain at different mesh sizes.

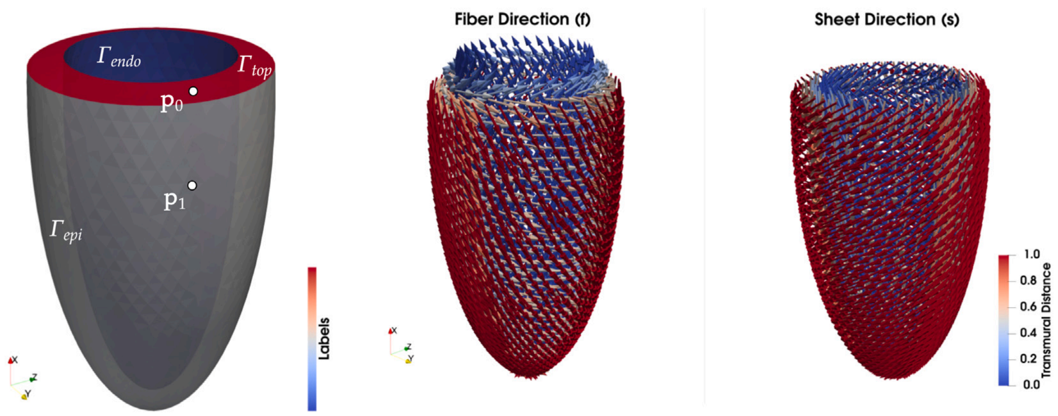

Fig. 1. The labeled ellipsoid geometry (left) includes positions of particles $\mathbf{p}_0, \mathbf{p}_1$ for reference. The fiber (center) and sheet (right) directions described in (15) for a $\mp 60°$ angle configuration, are colored using the transmural distance $\bar{t}$ over the domain. (For interpretation of the references to color in this figure legend, the reader is referred to the web version of this article.)

Table 1
Parameters describing the strong form of the problem defined in (1).

Parameter	$\rho\,[\frac{\text{kg}}{\text{m}^3}]$	$\eta\,[\text{Pas}]$	$\kappa\,[\text{Pa}]$	$k\,[-]$	$\alpha_{top}\,[\frac{\text{Pa}}{\text{m}}]$	$\alpha_{epi}\,[\frac{\text{Pa}}{\text{m}}]$	$\beta_{top}\,[\text{Pa}\,\frac{\text{s}}{\text{m}}]$	$\beta_{epi}\,[\text{Pa}\,\frac{\text{s}}{\text{m}}]$
Value	10^3	10^2	10^6	100	10^5	10^8	5×10^3	5×10^3

Table 2
Parameters of the constitutive law describing the directional behavior through fiber and sheet directions, described in (3).

Parameter	$a\,[\text{Pa}]$	$a_f\,[\text{Pa}]$	$a_{fs}\,[\text{Pa}]$	$a_s\,[\text{Pa}]$	$b[\cdot]$	$b_f[\cdot]$	$b_{fs}[\cdot]$	$b_s[\cdot]$
Value	59.0	18 472.0	216.0	2481.0	8.023	16.026	11.436	11.12

Table 3
Parameters defining the active stress activation function, solution to (5) and fibers' angles at endo/epi-cardium, as in [7].

Parameter	$\sigma_0\,[\text{Pa}]$	$\gamma\,[\text{s}]$	α_{min}	α_{max}	$t_{\text{sys}}\,[\text{s}]$	$t_{\text{dias}}\,[\text{s}]$	α_{endo}	α_{epi}
Value	1.5×10^5	0.005	-30	5	0.16	0.484	$-60°$	$+60°$

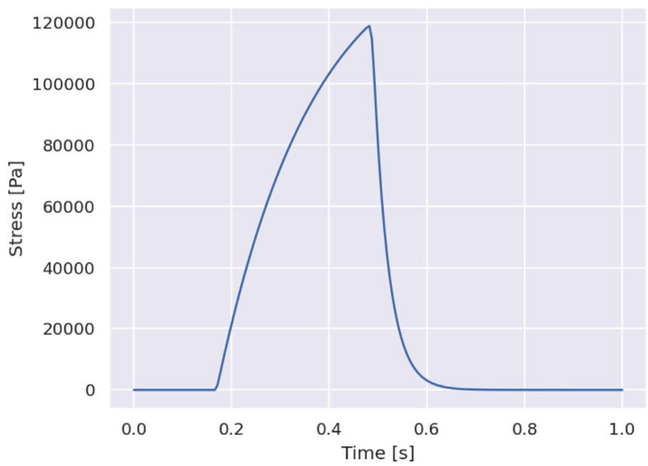

Fig. 2. Evolution of the stress function τ described in (5) over the time interval $[0, 1]$ with physiological parameters proposed in Table 3 from [7]. It reaches a maximum value of $118817.07\,[\text{Pa}]$.

3.3.2. Case B: Passive response

Each group solves numerically the equations described in Section 2 with geometry, fibers as in Sections 3.1, 3.2, and parameters as in Tables 1, 2, 4 and no active part, i.e. $\tau(t) = 0 \quad \forall t > 0$. The groups are requested to provide the displacement field $\mathbf{u}_h(\mathbf{X})$ over time at $\mathbf{p}_0, \mathbf{p}_1$.

Table 4
Parameters for the pressure model (7).

Parameter	Values
α_{min} [−]	−30
α_{max} [−]	5
α_{pre} [−]	5
α_{mid} [−]	1
σ_{pre} [Pa]	7000
σ_{mid} [Pa]	16 000
$t_{sys-pre}$ [s]	0.17
$t_{dias-pre}$ [s]	0.484
γ [s]	0.005

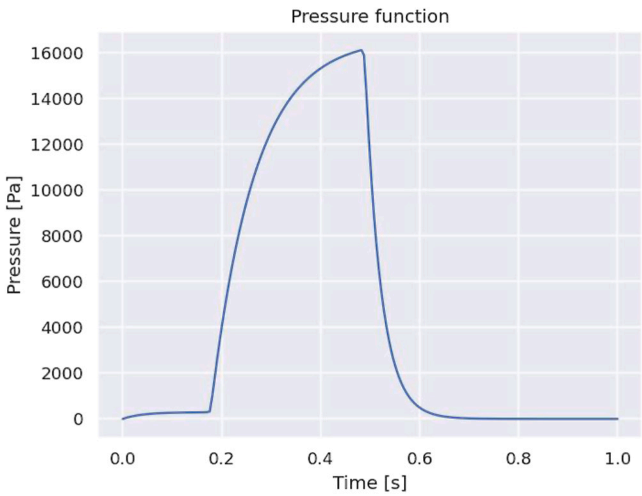

Fig. 3. Evolution of the pressure $p(t)$ described in (7) over the time interval $[0,1]$. Parameters as in Table 4. It reaches a maximum of 16117.52 [Pa].

Table 5
Each case combines a change in stiffness parameters a, a_f, a_{fs}, a_s with changes in the contractibility parameter σ_0.

Setup	a	a_f	a_{fs}	a_s	σ_0
Case A	177	55 416	648	7443	2×10^5
Case B	295	92 360	1080	12 405	1×10^5
Case C	19	6157	72	827	2×10^5

Depicted in Fig. 3 is the evolution of the pressure $p(t)$ over time for the parameters specified therein.

3.4. Step 1 (non-blinded): active and passive response

Each group solves numerically the equations described in Section 2 with geometry, fibers as in Sections 3.1, 3.2 and parameters as in Tables 1, 2, 3, 4. The groups are requested to provide the displacement field $\mathbf{u}_h(\mathbf{X})$ over time at two spatial locations, $\mathbf{p}_0$, $\mathbf{p}_1$, as described in Section 3.3.1.

3.5. Step 2: Blinded variation of physical parameters

In the second step, all groups are requested to run computations – fully blinded from each other – with modified physical constants with respect to Section 3.4. As an exception, the results computed with Simvascular were obtained non-blinded, meaning that they were produced after all other groups shared theirs. Here we changed a specific combination of parameters, namely a, a_f, a_{fs}, a_s by a constant factor and σ_0. The values taken for each parameter combination are given in Table 5, accounting for 3 different cases. The values have been chosen to get noticeably different results among the proposed cases and to challenge the robustness of the solvers.

Each group is requested to compute the displacement field at points $\mathbf{p}_0$, $\mathbf{p}_1$ for each case.

4. Benchmark 2: biventricular mechanics (blinded)

4.1. Strong formulation

Let us consider an idealized biventricular domain $\Omega \subset \mathbb{R}^3$ with boundaries $\partial\Omega := \Gamma_{endo-lv} \cup \Gamma_{endo-rv} \cup \Gamma_{epi} \cup \Gamma_{top}$. We denote by $\mathbf{u} : \Omega \to \mathbb{R}^3$ the displacement field, $\mathbb{T} := \mathbb{T}(\mathbf{u})$ the stress tensor as in Section 2.2 and $p_{lv}(t), p_{rv}(t)$ for each $t > 0$ pressure terms solving (7), with parameters to be specified below. We define the remaining operators $\mathbb{F}, J$ as in Section 2. The problem to solve is described by the equations:

$$\begin{aligned}
\rho\ddot{\mathbf{u}} - \mathbf{Div}(J\mathbb{T}\mathbb{F}^{-\top}) = \mathbf{0} \quad & \text{in } \Omega \\
J\mathbb{T}\mathbb{F}^{-\top}\mathbf{N} = p_{lv}J\mathbb{F}^{-\top}\mathbf{N} \quad & \text{on } \Gamma_{endo-lv} \\
J\mathbb{T}\mathbb{F}^{-\top}\mathbf{N} = p_{rv}J\mathbb{F}^{-\top}\mathbf{N} \quad & \text{on } \Gamma_{endo-rv} \\
J\mathbb{T}\mathbb{F}^{-\top}\mathbf{N}\cdot\mathbf{N} + \alpha_{epi}\mathbf{u}\cdot\mathbf{N} + \beta_{epi}\dot{\mathbf{u}}\cdot\mathbf{N} = 0 \quad & \text{on } \Gamma_{epi} \\
J\mathbb{T}(\mathbb{F}^{-\top}\mathbf{N})\times\mathbf{N} = \mathbf{0} \quad & \text{on } \Gamma_{epi} \\
J\mathbb{T}\mathbb{F}^{-\top}\mathbf{N} + \alpha_{top}\mathbf{u} + \beta_{top}\dot{\mathbf{u}} = \mathbf{0} \quad & \text{on } \Gamma_{top}
\end{aligned} \tag{17}$$

4.2. Geometry

To define the geometry we will introduce some notation. Given $\mathbf{x}_{cen} \in \mathbb{R}^3$ and $\{a, b, c\} \in \mathbb{R}_+$, we define $V(\mathbf{x}_{cen}, (a, b, c)) \subset \mathbb{R}^3$ an ellipsoidal domain, centered at $\mathbf{x}_{cen}$ with (a, b, c) the length of each $(\hat{x}, \hat{y}, \hat{z})$ semiaxis, $\partial V(\mathbf{x}_{cen}, (a, b, c))$ its boundary.

The biventricular domain $\Omega \subset \mathbb{R}^3$ is characterized by four different surfaces:

- Epicardial surface (Γ_{epi}) described as a set of points $\mathbf{x} = (x, y, z) \in \mathbb{R}^3$ satisfying
$$\begin{aligned}
&\mathbf{x} \in \partial V\left(\mathbf{0}, (a_{\text{lv-epi}}, b_{\text{lv-epi}}, c_{\text{lv-epi}})\right) \Delta \partial V\left(\mathbf{x}_{\text{rv}}, (a_{\text{rv-epi}}, b_{\text{rv-epi}}, c_{\text{rv-epi}})\right) \\
&\quad \mathbf{x} \text{ s.t. } x < 0
\end{aligned} \tag{18}$$
for $\mathbf{x}_{rv} = (0, 0, 0.02)$ and centers $(a_{\text{lv-epi}}, b_{\text{lv-epi}}, c_{\text{lv-epi}}) = (0.08, 0.039, 0.039)$ and $(a_{\text{rv-epi}}, b_{\text{rv-epi}}, c_{\text{rv-epi}}) = (0.075, 0.038, 0.059)$.
- Left endocardial surface ($\Gamma_{endo-lv}$) described as the set $\mathbf{x} = (x, y, z) \in \mathbb{R}^3$ satisfying
$$\begin{aligned}
&\mathbf{x} \in \partial V\left(\mathbf{0}, (a_{\text{lv-endo}}, b_{\text{lv-endo}}, c_{\text{lv-endo}})\right) \\
&\quad \mathbf{x} \text{ s.t. } x < 0
\end{aligned} \tag{19}$$
for $(a_{\text{lv-endo}}, b_{\text{lv-endo}}, c_{\text{lv-endo}}) = (0.069, 0.025, 0.025)$.
- Right endocardial surface ($\Gamma_{endo-rv}$) described as the set $\mathbf{x} = (x, y, z) \in \mathbb{R}^3$ satisfying
$$\begin{aligned}
&\mathbf{x} \in \partial V\left(\mathbf{x}_{rv}, (a_{\text{rv-endo}}, b_{\text{rv-endo}}, c_{\text{rv-endo}})\right) \\
&\quad \mathbf{x} \text{ s.t. } x < 0
\end{aligned} \tag{20}$$
for $(a_{\text{rv-endo}}, b_{\text{rv-endo}}, c_{\text{rv-endo}}) = (0.07, 0.033, 0.054)$.
- Base (Γ_{top}) as the set $\mathbf{x} = (x, y, z) \in \bar{\Gamma}_{epi} \cup \bar{\Gamma}_{\text{endo-lv}} \cup \bar{\Gamma}_{\text{endo-rv}}$ s.t. $x = 0$

The proposed geometry is depicted in Fig. 4.

4.3. Fibers

For the fiber directions, we use a Laplace–Dirichlet Rule-Based (BT-LDRB) algorithm [34], modified to adhere to the convention utilized for the cross-fiber orientations.[5] We take a values of $\mp 60°$ (with respect to a local coordinate system) for the left and right endo/epi- cardial fiber angles.[6]

The fibers are created using the `life`$^{\text{x}}$ software [41,42]. Fig. 5 depicts the step-by-step procedure to prescribe the fiber architecture in the biventricular geometry [34,41]. For further details refer to [34].

4.4. Physical constants and evaluation of results

Each group is requested to solve problem (17) with parameters as in Tables 2, 7, 8, , with geometry and fibers as in Sections 4.2, 4.3, for two refinement levels.[7] Table 6 details the number of tetrahedra and nodes:

---

[5] In the last decades, myocardial orientation has been studied from histological data [18,35] and *Diffusion Tensor Imaging* [36,37], but their reconstructed noisy data suffers from low resolution, limiting its characterization, especially given the thickness of ventricles, which is usually smaller than the voxel size [38]. Several construction algorithms have been proposed to recreate the fiber orientation, ranging from complex registration data-dependent algorithms to *Rule-Based Methods*, which remains an active area of research [34,39,40].

[6] The convention in this work entails switching the directions $\mathbf{s}$ and $\mathbf{n}$ in relation to the formalism entailed in the state-of-the-art [34].

[7] The repository cardiac-benchmark-toolkit stores the biventricular domain in several formats `.geo`, `.msh`, `.xdmf`, `.h5`.

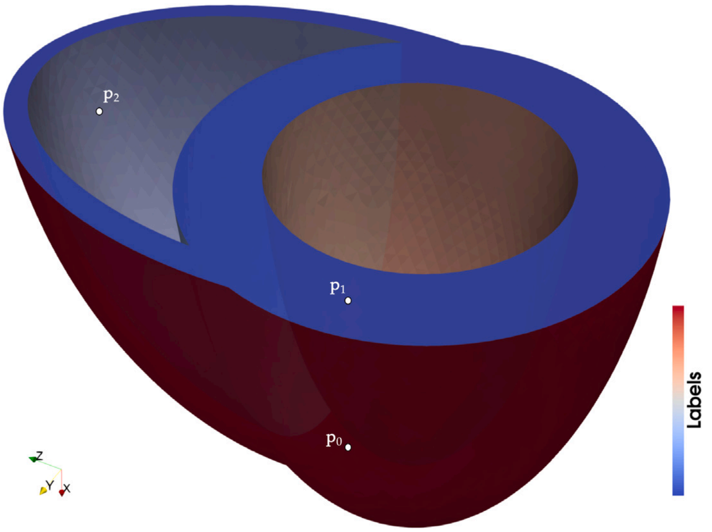

Fig. 4. Geometry for the biventricular domain with colored boundaries: $\Gamma_{epi}, \Gamma_{endo-lv}, \Gamma_{endo-rv}$ and Γ_{top}. Positions of particles of interest $\mathbf{p}_0, \mathbf{p}_1$ and $\mathbf{p}_2$ are depicted with circles for reference. (For interpretation of the references to color in this figure legend, the reader is referred to the web version of this article.)

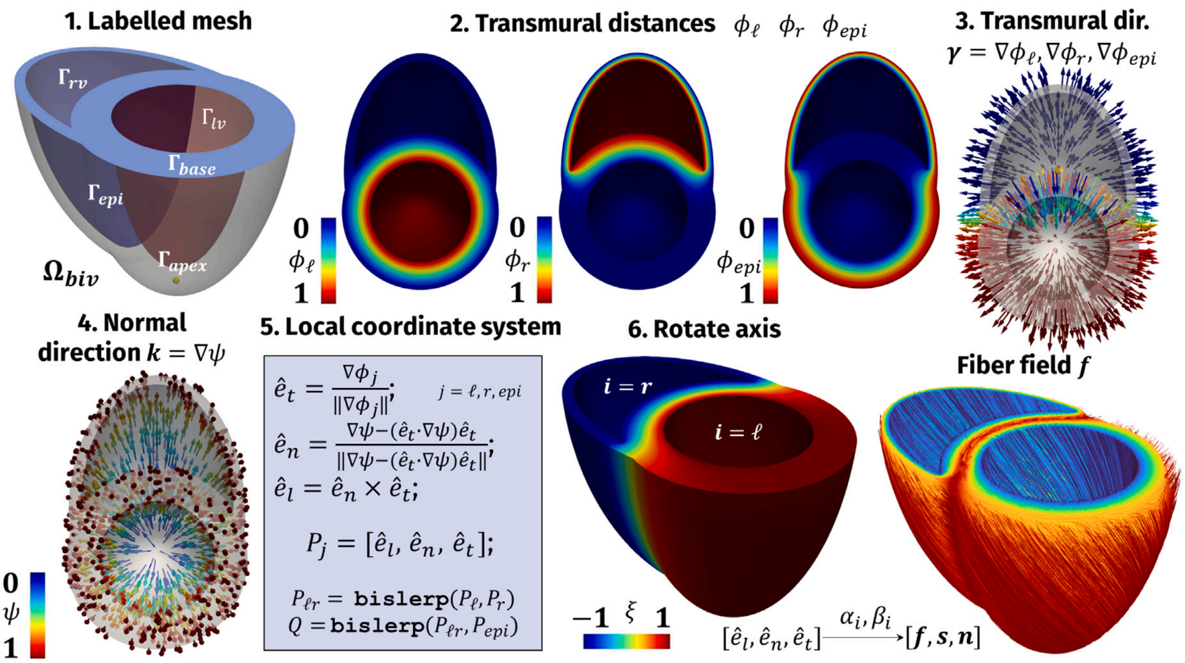

Fig. 5. Step-by-step procedure for the fiber architecture. In 1. labeled mesh with boundaries, 2. transmural distances $\phi_l, \phi_r, \phi_{epi}$, 3. transmural directions $\gamma = \nabla\phi_l, \nabla\phi_r, \nabla\phi_{epi}$, 4. normal direction $k = \nabla\psi$, 5. local coordinate definition $\hat{e}_t, \hat{e}_n, \hat{e}_l$, 6. rotation of axis and fiber field system $[\mathbf{f}, \mathbf{s}, \mathbf{n}]$. (For interpretation of the references to color in this figure legend, the reader is referred to the web version of this article.)

Extending Step 2 of Benchmark 1, groups are requested to provide displacement fields $\mathbf{u}_h(\mathbf{X})$ over time at three spatial locations $\mathbf{p}_0 = (0.025, 0.03, 0), \mathbf{p}_1 = (0, 0.03, 0), \mathbf{p}_2 = (0.025, 0, 0.072)$.

Depicted in Figs. 6 and 7 are the time-evolution of the activation function and pressure curves with parameters specified therein.

Table 6
Number of tetrahedra and nodes for two refinement levels, denoted by Ω_{h_1} and Ω_{h_2}.

Mesh	Num. of tetrahedra	Num. of nodes
Ω_{h_1}	45,304	11,444
Ω_{h_2}	121,133	27,807

Table 7
Parameters describing the strong form of the problem defined in (17).

Parameter	$\rho\,[\frac{\text{kg}}{\text{m}^3}]$	η [Pa s]	κ [Pa]	k [−]	$\alpha_{top}\,[\frac{\text{Pa}}{\text{m}}]$	$\alpha_{epi}\,[\frac{\text{Pa}}{\text{m}}]$	$\beta_{top}[\text{Pa}\,\frac{s}{m}]$	$\beta_{epi}\,[\text{Pa}\,\frac{\text{s}}{\text{m}}]$
Value	10^3	10^2	10^6	100	10^6	10^8	5×10^3	5×10^3

Table 8
Parameters defining the active stress activation function, solution to (5), for the biventricular model.

Parameter	σ_0 [Pa]	γ [s]	$\alpha_{\min}$	$\alpha_{\max}$	t_{sys} [s]	t_{dias} [s]
Value	1.5×10^5	0.005	−30	5	0.163	0.5

Table 9
Left table: parameters used for $p_{lv}(t)$, so that it attains a maximum of 16491.14 [Pa] $\approx$ 123 [mmHg]. Right: parameters used for $p_{rv}(t)$ with a maximum of 4166.66 [Pa] $\approx$ 31 [mmHg].

Parameter (p_{lv})	Value	Parameter (p_{rv})	Value
$\alpha_{min}[\cdot]$	−30	$\alpha_{min}[\cdot]$	−30
$\alpha_{max}[\cdot]$	5	$\alpha_{max}[\cdot]$	5
$\alpha_{pre}[\cdot]$	5	$\alpha_{pre}[\cdot]$	1
$\alpha_{mid}[\cdot]$	15	$\alpha_{mid}[\cdot]$	10
σ_{pre} [Pa]	12 000	σ_{pre} [Pa]	3000
σ_{mid} [Pa]	16 000	σ_{mid} [Pa]	4000
$t_{sys-pre}$ [s]	0.17	$t_{sys-pre}$ [s]	0.17
$t_{dias-pre}$ [s]	0.484	$t_{dias-pre}$ [s]	0.484
γ [s]	0.005	γ [s]	0.005

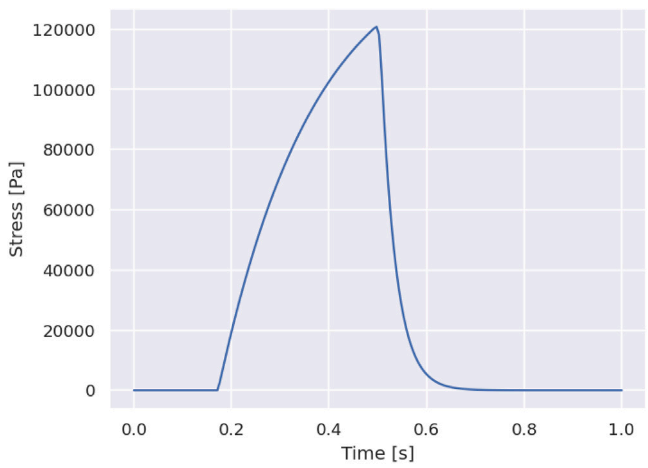

Fig. 6. Evolution of the stress function τ described in (5) over the time interval $[0,1]$ with parameters as in Table 8. It reaches a maximum value of 120775.56 [Pa].

5. Numerical solvers and participants

Each group was requested to disclose their strategies to solve problems (1) and (17). Settings for the software, spatial and temporal discretization methods are described in Table 10. The notation $\mathbb{P}_2$ indicates that the incompressibility is handled via penalization (as described in the previous sections), and therefore only the displacements are discretized with quadratic basis

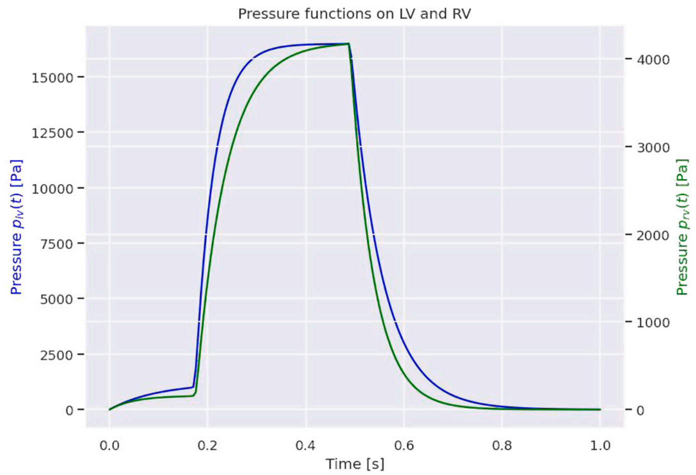

Fig. 7. Evolution of pressure $p_{lv}(t), p_{rv}(t)$ are shown with blue and brown colors respectively over the time interval $[0, 1]$. Parameters as in Table 4. Maximum values of $16491.15\,[\mathrm{Pa}]$ and $4171.07\,[\mathrm{Pa}]$ for p_{lv}, p_{rv} respectively. (For interpretation of the references to color in this figure legend, the reader is referred to the web version of this article.)

Table 10
Summary table of strategies. All problems are solved using the Newton method. Notation: Gen-α denotes the generalized-α scheme [43] and KGen-α an subclass of Gen-α with specific spectral properties [44]. GL denotes the Gauss–Legendre and KL the Keast Lyness quadrature rules, respectively. FEniCSx [45–47] is the succesor of FEniCS [48–50]. In the linear solver column, teams differ between linear algebra backend such as MUMPS [51], SuperLU [52], PETSc [53], Trilinos [54] and PARDISO [55], to solve the linear system of the newton step.

Affiliation	Software	Spatial discr.	Quad. type – degree	Linear solver	Time discretization
Medical University of Graz	CARPentry [56]	$\mathbb{P}_1$-$\mathbb{P}_1$ [57]	KL - 6	GMRES [58] with GAMG precond	KGen-α with spectral radius $\rho_\infty = 0.5$, timestep at 1 [ms]
King's College London	Ambit [59] (FEniCSx)	$\mathbb{P}_2$	GL - 6	LU [51] for bench. 1 and GMRES with AMG precond. [53] for bench. 2	Gen-α with $\alpha_m = \alpha_f = 0, \beta = 0.25, \gamma = 0.5$, timestep at 1 [ms]
Technische Universit`at M'unchen	[4C] [60]	$\mathbb{P}_2$	GL - 4 (stiffness), 11 (mass)	GMRES with AMG precond.	Gen-α with $\alpha_m = \alpha_f = 0.5, \beta = 0.25, \gamma = 0.5$, timestep at 1 [ms].
Simula Research	FEniCS [61]	$\mathbb{P}_2$	GL - 6	LU [52]	Gen-α with $\alpha_m = 0.2, \alpha_f = 0.4$, timestep at 1 [ms].
University of Groningen	CHIMeRA (FEniCS)	$\mathbb{P}_2$	GL - 6	LU [51]	Gen-α with $\alpha_m = \alpha_f = 0$, $\beta = 0.25, \gamma = 0.5$, timestep at 1 [ms].
University of Michigan	$\mathcal{C}$Heart [62]	$\mathbb{P}_2$	KL - 4	LU [51]	Mid-point rule, timestep at 1 [ms]
Politecnico di Milano	life^x [41]	$\mathbb{P}_2$	GL - 4	GMRES with AMG precond.	BDF1 Implicit, timestep at 1 [ms].
Technische Universiteit Delft	COMSOL Multiphysics v.6.1 [11,63,64]	$\mathbb{P}_2$	GL - 4	LU [55]	Gen-α with $\alpha_m = \alpha_f = 0$, $\beta = 0.25, \gamma = 0.5$, timestep at 1 [ms]
Columbia University	SimVascular [svFSI] [65–67]	$\mathbb{P}_1$-$\mathbb{P}_1$	GL - 4	GMRES with Schwarz Prec. (bench. 1) and GMRES with iLU [54] (bench. 2)	KGen-α with spectral radius $\rho_\infty = 0.5$, timestep at 1 [ms]
Columbia University	SimVascular [svFSI] [65–67]	$\mathbb{P}_2$	GL - 11	GMRES with AMG Precond. for bench. 1	idem

functions. The notation $\mathbb{P}_1$ indicated the analogous case for linear basis functions. The notation $\mathbb{P}_1 - \mathbb{P}_1$ indicates that incompressibility is handled directly using the pressure as unknown, where the saddle-point problem is discretized with linear basis functions, including a stabilization term for the pressure field. This variable, defined in the muscle, differs from the pressure prescribed at the boundaries, describing chamber and epicardial effects.

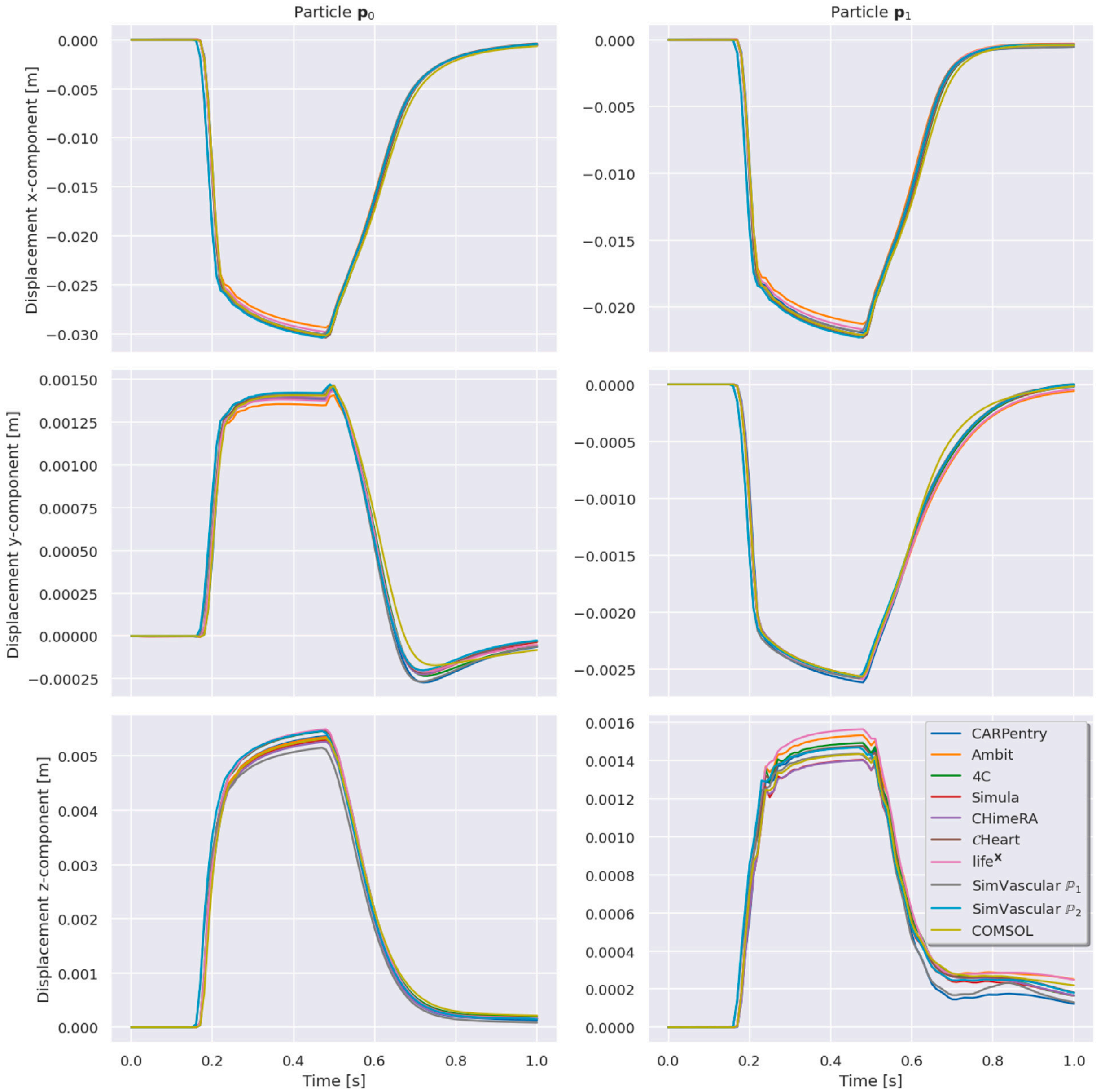

Fig. 8. Comparison per component of displacement $\mathbf{u}_h(\mathbf{p}_0)$ and $\mathbf{u}_h(\mathbf{p}_1)$ for Step 0, case A - active response. (For interpretation of the references to color in this figure legend, the reader is referred to the web version of this article.)

6. Results

In this section, we provide comparison results for the two benchmark problems. Quantitative and qualitative assessment is done using displacement tracking and by defining a measure of discrepancy between teams. Solutions from different teams can be distinguished with different colors, which are provided in displacement curves for benchmark 1 and including visualizations for benchmark 2. Comparisons between $\mathbb{P}_1$ and $\mathbb{P}_2$ are also provided for benchmark 2.

6.1. Benchmark 1

6.1.1. Step 0 (non-blinded): Splitting passive and active response

The comparison of displacement curves at particles $\mathbf{p}_0, \mathbf{p}_1$ is depicted in Fig. 8 for active response alone and in Fig. 9 for passive response. Each figure presents displacements for each of the component, allowing a straightforward assessment of differences

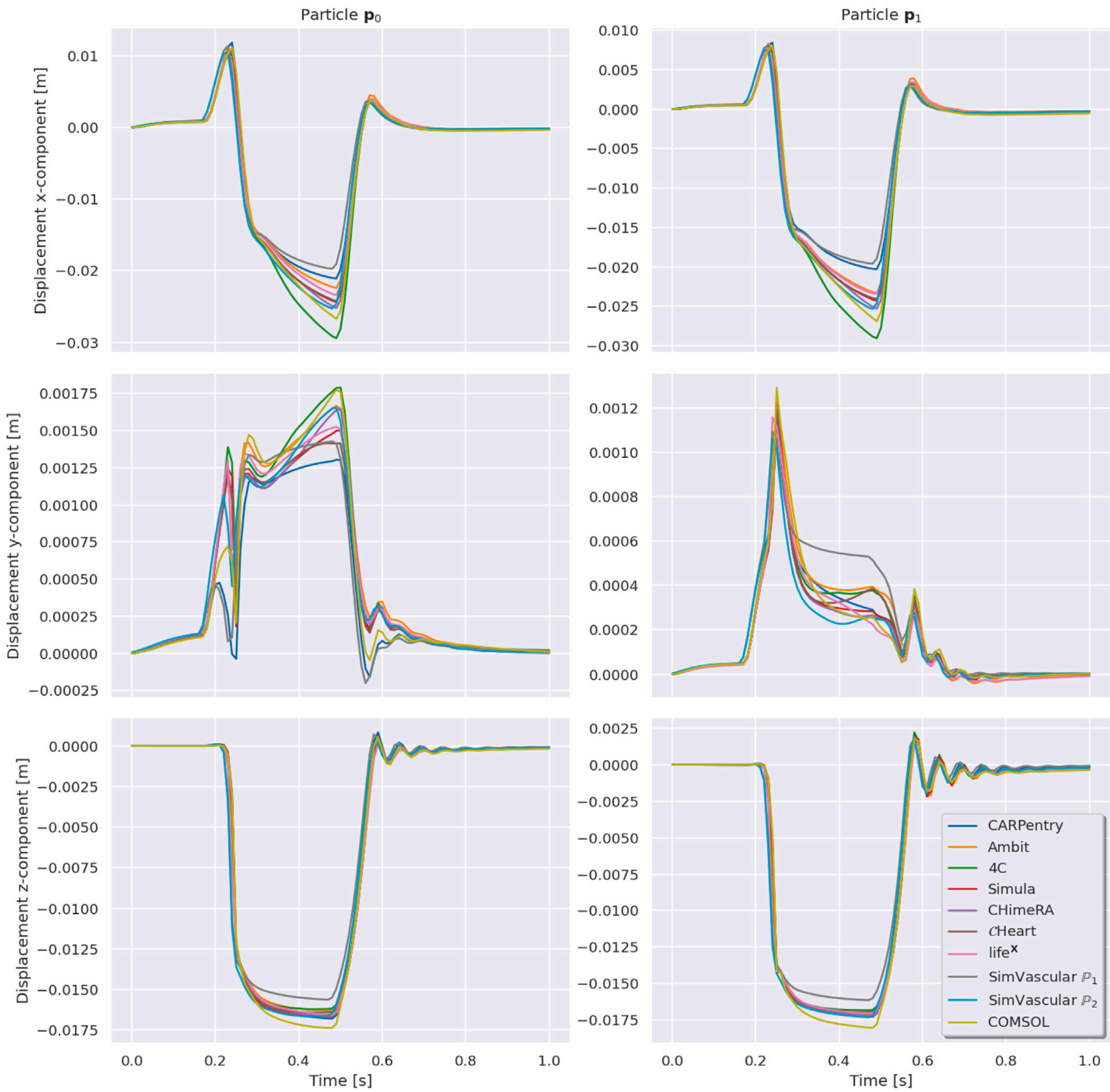

Fig. 9. Comparison per component of displacement $\mathbf{u}_h(\mathbf{p}_0)$ and $\mathbf{u}_h(\mathbf{p}_1)$ for Step 0, case B - passive response. (For interpretation of the references to color in this figure legend, the reader is referred to the web version of this article.)

between teams. The largest differences can be observed primarily along the interval $(0.2, 0.6)$ [s], and especially for the x-component of both particles in the case of passive response.

6.1.2. Step 1 (non-blinded): active and passive response

The comparison results for each requested quantity are depicted in Fig. 10. The componentwise representation of displacement showcases the differences in the order of magnitude of deformation. Displacements along the z-component are one order of magnitude smaller than those of the x-component. Maximum differences between teams remain smaller than 0.5 [mm] in the worst case, as seen in the z-component.

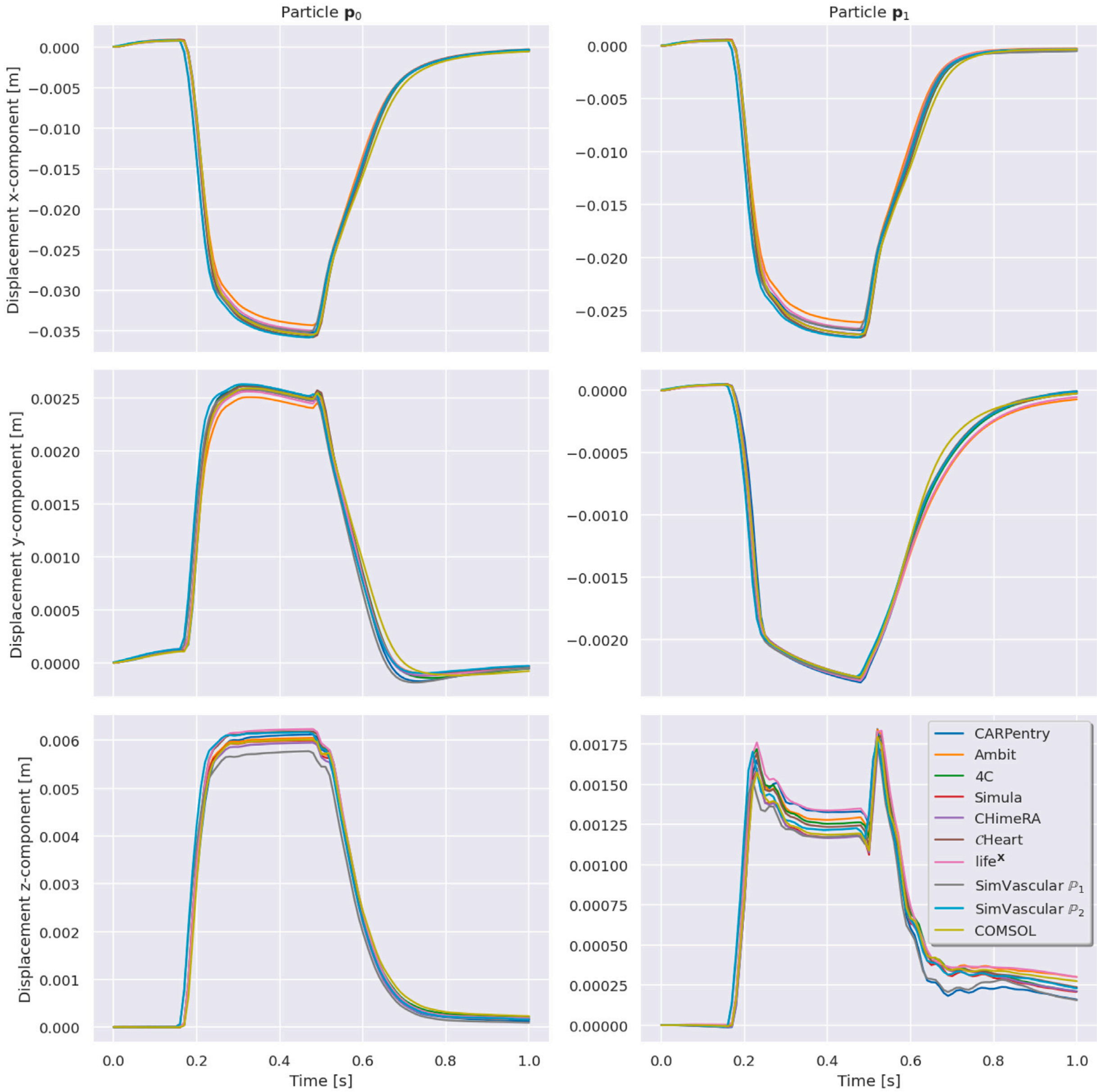

Fig. 10. Comparison per component of displacement $\mathbf{u}_h(\mathbf{p}_0)$ and $\mathbf{u}_h(\mathbf{p}_1)$ for Step 1, case of joint active and passive response. (For interpretation of the references to color in this figure legend, the reader is referred to the web version of this article.)

6.1.3. Step 2

A qualitative comparison of displacement curves at different particles is depicted in Figs. 11–13. For a quantitative assessment of the curves, we propose a [RE]lative [D]iscrepancy between each dataset, denoted by RED, defined as:

$$\mathtt{RED}(\mathbf{p}) = \frac{1}{T} \sum_{t_n=0}^{T} \frac{\|\mathbf{u}(t_n, \mathbf{p}) - \bar{\mathbf{u}}(t_n, \mathbf{p})\|_{\ell^2}}{\|\bar{\mathbf{u}}(t_n, \mathbf{p})\|_{\ell^2}} \quad \mathbf{p} \in \{\mathbf{p}_0, \mathbf{p}_1\} \tag{21}$$

with $\bar{\mathbf{u}}(t,\cdot) = \frac{1}{N}\sum_{i=1}^{N} \mathbf{u}^i(t,\cdot)$ for $t \in (0,1)$, $\mathbf{u}^i$ the displacement field of team i and N the total number of teams. The datasets are subsampled at $10\,[\mathrm{ms}]$, i.e. $T = 101$ datapoints. If a group simulated with a different timestep, then linear interpolation is used to compute the corresponding displacement values. Intuitively, the relative discrepancy function provides a time-averaged discrepancy to an average result, using the ℓ^2 norm to add each direction. Table 11 summarizes the relative discrepancies for each team.

Table 11
Comparison of relative deviations for each participant group.

Setup	Case A		Case B		Case C	
	RED ($\mathbf{p}_0$)	RED ($\mathbf{p}_1$)	RED ($\mathbf{p}_0$)	RED ($\mathbf{p}_1$)	RED ($\mathbf{p}_0$)	RED ($\mathbf{p}_1$)
CARPentry	0.134	0.229	0.360	0.301	0.060	0.118
Ambit	0.115	0.185	0.79	0.243	0.060	0.168
4C	0.080	0.115	0.171	0.136	0.059	0.059
Simula	0.094	0.200	0.311	0.352	0.041	0.054
CHIMeRA	0.078	0.108	0.149	0.135	0.045	0.056
$\mathcal{C}$Heart	0.202	0.198	0.300	0.250	0.048	0.045
life^x	0.108	0.154	0.273	0.252	0.049	0.129
SimVascular $\mathbb{P}_1$	0.220	0.371	0.309	0.267	0.156	0.211
SimVascular $\mathbb{P}_2$	0.276	0.370	0.360	0.328	0.146	0.157
COMSOL	0.186	0.196	0.287	0.329	0.105	0.111

Table 12
Comparison of relative deviations for each participant group in Benchmark 2.

Setup	Blinded on Ω_{h_1}			Blinded on Ω_{h_2}		
	RED ($\mathbf{p}_0$)	RED ($\mathbf{p}_1$)	RED ($\mathbf{p}_2$)	RED ($\mathbf{p}_0$)	RED ($\mathbf{p}_1$)	RED ($\mathbf{p}_2$)
CARPentry	0.915	0.545	0.415	1.019	0.504	0.452
Ambit	0.094	0.086	0.21	0.136	0.084	0.288
4C	0.104	0.129	0.221	0.108	0.094	0.278
Simula	0.564	0.848	1.472	0.446	0.513	1.769
CHIMeRA	0.121	0.108	0.182	0.111	0.079	0.347
$\mathcal{C}$Heart	0.144	0.11	0.226	0.137	0.085	0.406
life^x	0.125	0.099	0.144	0.103	0.077	0.318
SimVascular $\mathbb{P}_1$	0.483	0.295	0.95	0.294	0.184	0.508
COMSOL	0.14	0.158	0.335	0.183	0.155	0.326

6.2. Benchmark 2

To analyze the results, qualitative assessment is done through visual inspection and the displacement tracking at three particles $\mathbf{p}_0, \mathbf{p}_1$ and $\mathbf{p}_2$. We provide quantitative assessment using the measure of discrepancy RED, as in Section 6.1.3, for all particles in both meshes. Visual comparison between solutions can be depicted in Fig. 14 using overlapped views at two different times, namely, 0.3 [s] and 0.5 [s]. The views are defined using the two-chamber (long) axis and the base-to-apex (short) axis. Particle trajectories are depicted in Figs. 15 for the coarse mesh Ω_{h_1} and 16 for the fine mesh Ω_{h_2}. Table 12 summarizes the discrepancies in each case. Comparison curves between spatial discretization in $\mathbb{P}_1$ and $\mathbb{P}_2$ are depicted in Figs. 17 and 18, including only teams that provided both datasets.

7. Discussion

This work proposes a set of benchmark problems and solutions for cardiac elastodynamics, in both, monoventricular and biventricular geometries. Evaluation of the solutions is done both qualitatively (from the time evolution of displacements) and quantitatively (using the discrepancy measure RED).

The benchmarks proposed here not only assess nonlinear elastodynamics but also test active material behavior and pericardial boundary conditions [7]. They also showcase the potential variability in the results from different numerical approaches used by the cardiac biomechanics community. This work not only provides the analytical description for the monoventricular case, as done in [2], but also utilizes the state-of-the-art fiber generation pipeline [34] for the biventricular domain.

This report provides an unambiguous mathematical description of cardiac benchmark problems, sufficient for reproducibility purposes with a reasonable agreement of solutions between teams for all proposed problems. In total, nine different research groups submitted solutions to the benchmark problems, all computed with the finite element method but with different approaches to handle (in)compressibility, see Table 10.

The monoventricular benchmark case comprises three different problems that aim to assess separately passive 3.3.2 and active 3.3.1 responses of the cardiac contractility, as well as their combined effect 3.4. In the non-blinded phase, teams had access to numerical solutions provided by other participants. In this phase, solutions agree closely on the active, passive and joint responses, as depicted in Figs. 8–10. The difference between curves is below 0.5 [mm], only a small fraction of the typical element size employed (3–5 [mm]). The largest differences are observed when the discrete system is passively loaded as seen in Table 11.

In the blinded-phase, teams tested their numerical setup in three new sets of parameters. The choice of parameters defines different material regimes, a high and low stiffness set of parameters (Case A and C, respectively), tuned to have physiological contraction and a third case tuned to have small deformations to test robustness of the solvers. In all cases, a reasonable agreement is observed among teams, as depicted in Figs. 11–13. This agreement is present despite some groups (SimVascular, CHIMeRA, $\mathcal{C}$Heart and life^x) using different ways to generate or interpolate the fiber directions, as summarized in Table 10.

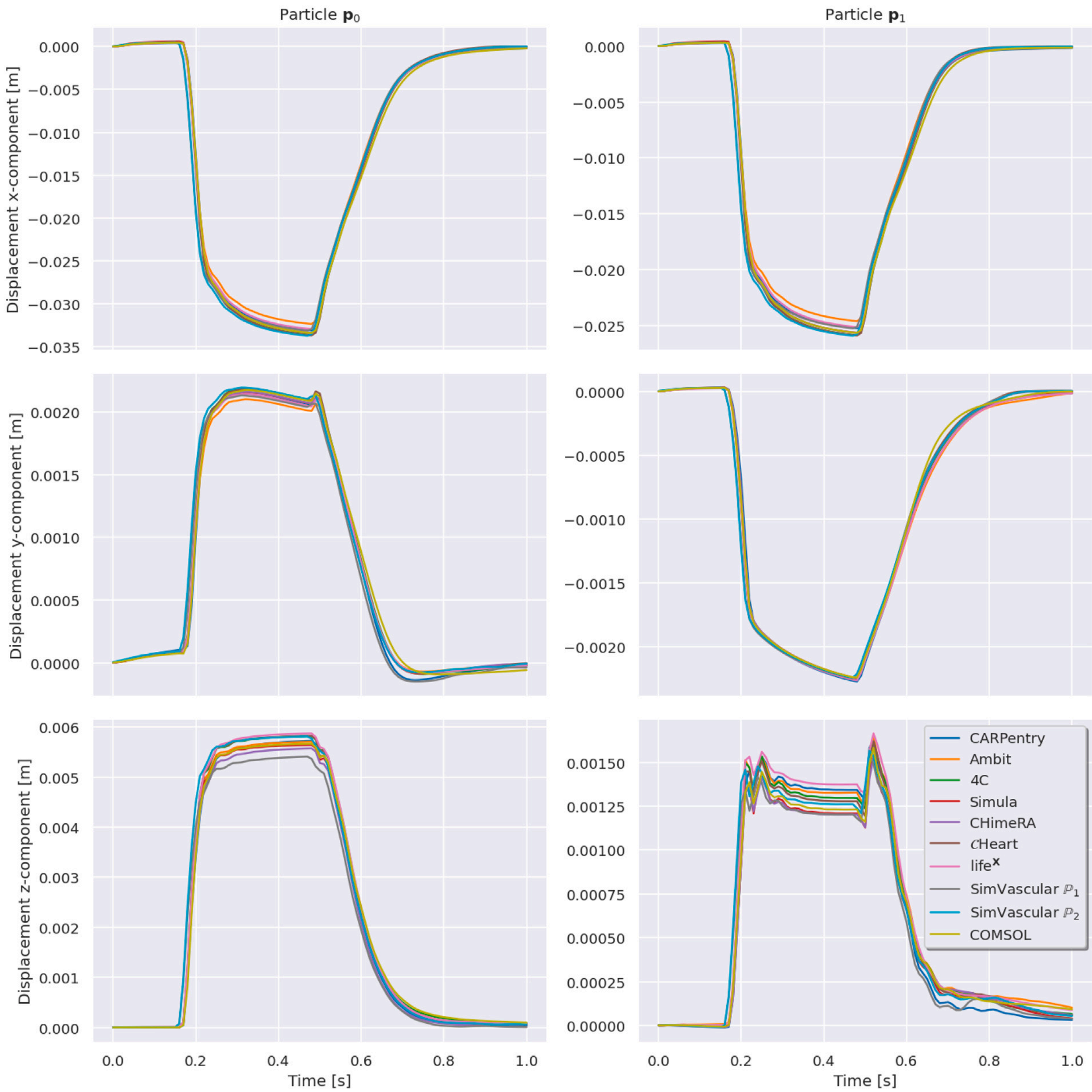

Fig. 11. Comparison per component of displacement $\mathbf{u}_h(\mathbf{p}_0)$ and $\mathbf{u}_h(\mathbf{p}_1)$, case A. (For interpretation of the references to color in this figure legend, the reader is referred to the web version of this article.)

The blinded biventricular case 4.4, aims to assess each solver in a more realistic scenario with a non-parametric fiber configuration and a generalized elastodynamic formulation. As depicted in Figs. 15 and 16, there is a closer match between results when using the finer mesh Ω_{h_2} compared to Ω_{h_1}. A qualitative comparison of the solutions along the short and long axis planes is depicted in Fig. 14. Greater discrepancy is observed between solutions based on $\mathbb{P}_1 - \mathbb{P}_1$ compared to $\mathbb{P}_2$ formulations. Discrepancies are noticeable across all particle displacements in the coarser mesh, particularly for the particle $\mathbf{p}_2$, reflecting the variability of the solutions across the mesh. Effects of the spatial discretization are also considered in this work. Comparisons between solution fields in $\mathbb{P}_1$ and $\mathbb{P}_2$, depicted in Figs. 17 and 18 for the coarse and fine mesh, showcase a dependency of the solution on the discretization space and to the fibers orientation, with differences larger than 5 [mm] in the interval $(0.2, 0.5)$ [s].

A close agreement between most of the groups in the monoventricular case (Table 11) using different software and methods. However, in the biventricular case, an increased discrepancy is evident (Table 12), even among the teams that used similar software

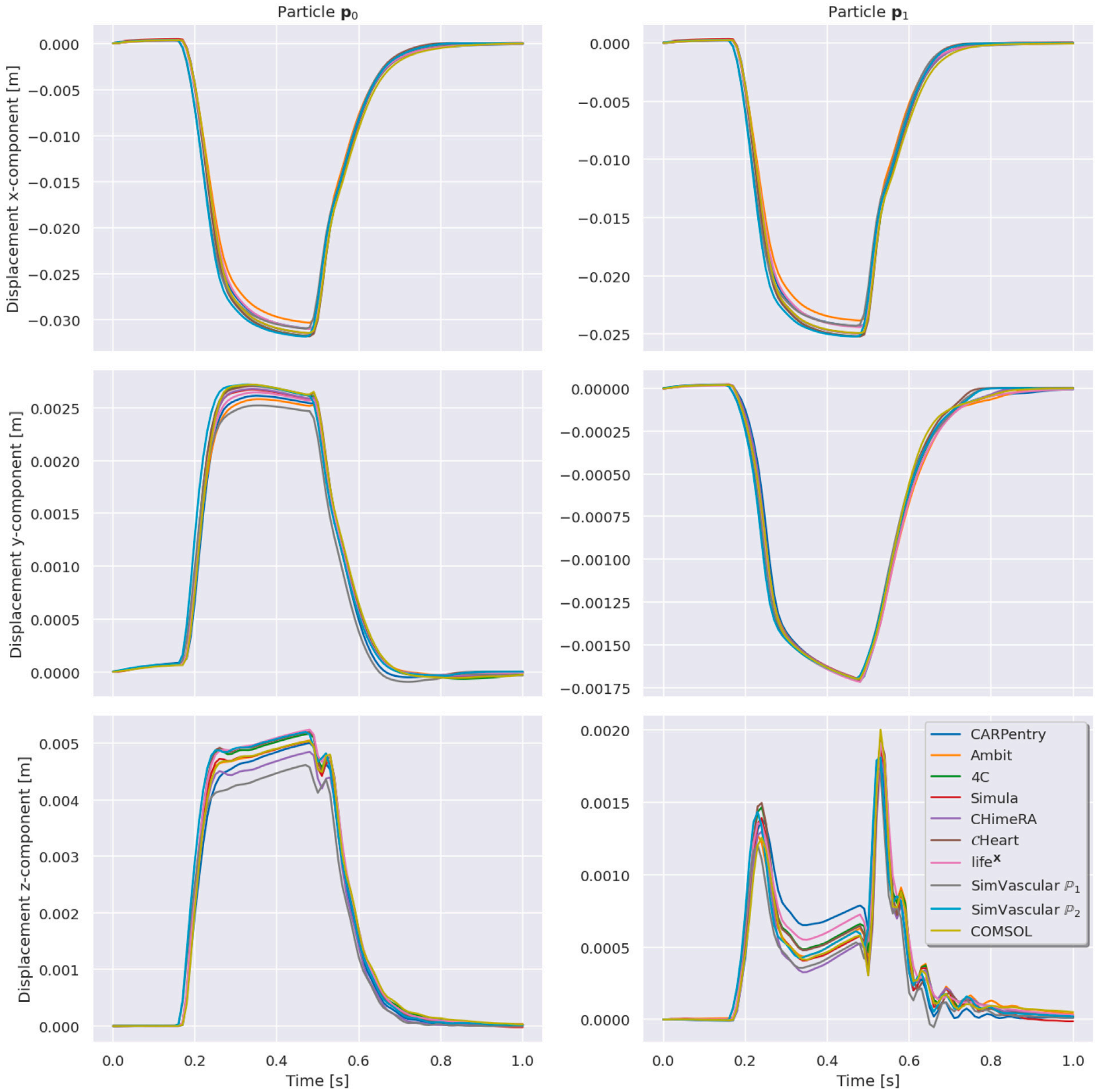

Fig. 12. Comparison per component of displacement $\mathbf{u}_h(\mathbf{p}_0)$ and $\mathbf{u}_h(\mathbf{p}_1)$, case B. (For interpretation of the references to color in this figure legend, the reader is referred to the web version of this article.)

platform, e.g. FEniCS (`Ambit`, `Simula`, `CHIMeRA`). This is likely due not only to differences in geometry but also to the rule-based calculation of fibers, which were provided at the degrees of freedom and then interpolated to the quadrature points. This interpolation process may introduce additional variability in the simulation outputs across the groups.

8. Limitations

This work presents a number of limitations that could be tackled in future studies.

Though this study represents a considerable improvement in modeling complexity, it still addresses only one physical field, namely mechanics. Including additional fields in a multiphysics framework – such as fluid-solid interaction, poromechanics, electromechanics, and 0D-3D models – would likely be the most reasonable next steps. However, this approach may reduce the number of groups participating in each of these benchmarks.

In principle, the observed differences may disappear if the discretization is refined to the point where all solvers reach convergence, but no detailed convergence analysis was performed in this study. At that stage, the comparison would focus primarily

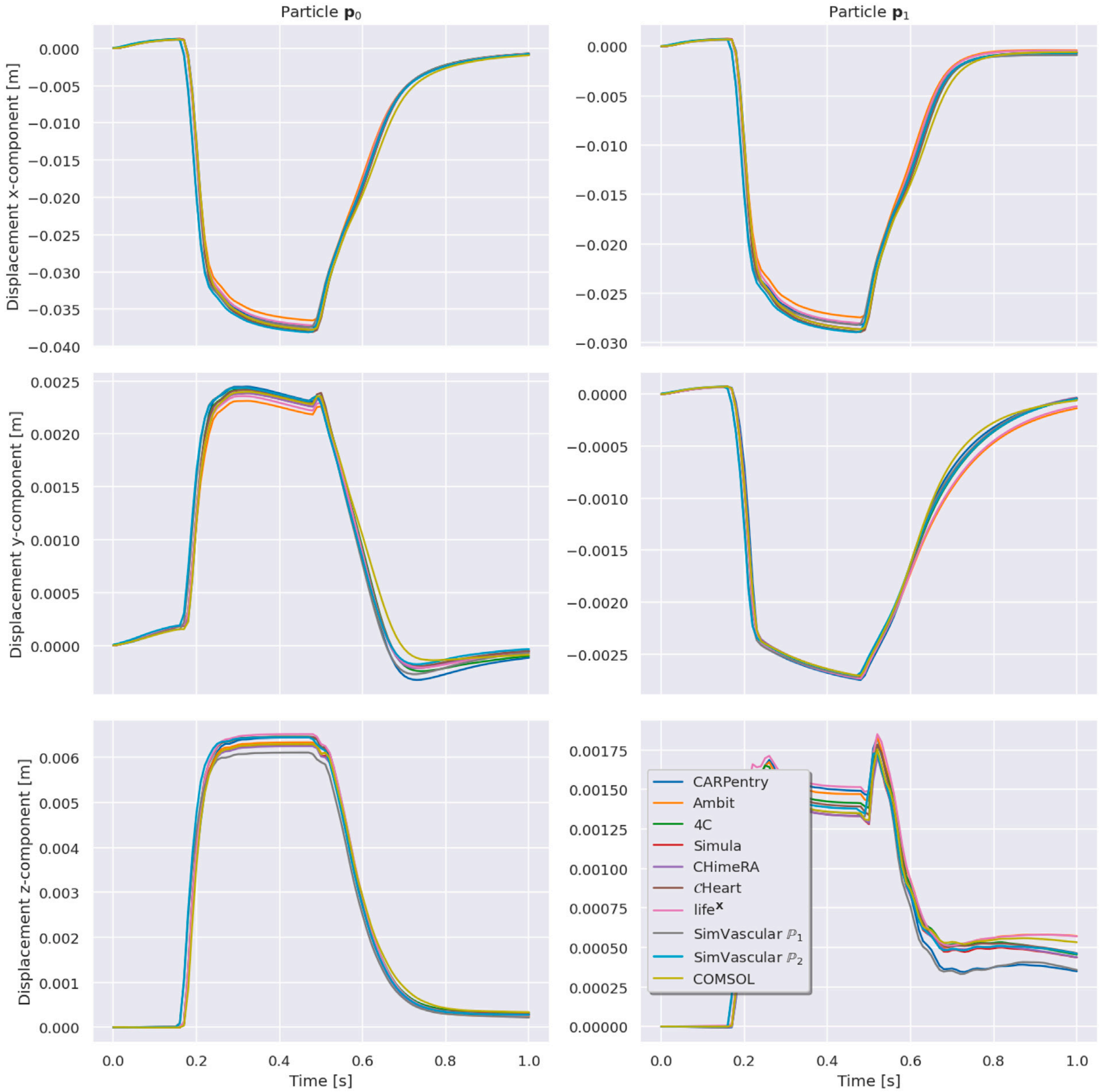

Fig. 13. Comparison per component of displacement $\mathbf{u}_h(\mathbf{p}_0)$ and $\mathbf{u}_h(\mathbf{p}_1)$, case C. (For interpretation of the references to color in this figure legend, the reader is referred to the web version of this article.)

on computational cost, assuming that, as one would hope, all the solvers converge to the same solution but with different accuracy orders.

The present work also has limitations regarding the realism of the fiber model. While the fiber-sheet-normal model is well established for left ventricular geometries, there is a lack of data for the right ventricle and interventricular region [68]. The benchmark could be updated with more realistic biventricular fiber models [34,69]. However, this is likely to introduce additional numerical challenges and require more careful discretization due to the thinness of the right ventricular wall.

While incorporating a human or animal geometry, especially one including the atria, is feasible in principle, it falls outside the scope of the proposed benchmark and would overly complicate the setup. Additionally, generating atrial fibers remains a significant challenge [34,70]. Therefore, given the focus of our work, we rely on idealized ventricular geometries paired with state-of-the-art fiber models. A more realistic and complex geometry could also lead to challenges in incorporating the fiber orientation and in the comparison and interpretation of the results. The current study seeks to achieve a balanced model complexity, which would render the results useful and relevant but still allow control of relevant model properties and facilitate the comparison of the results. The

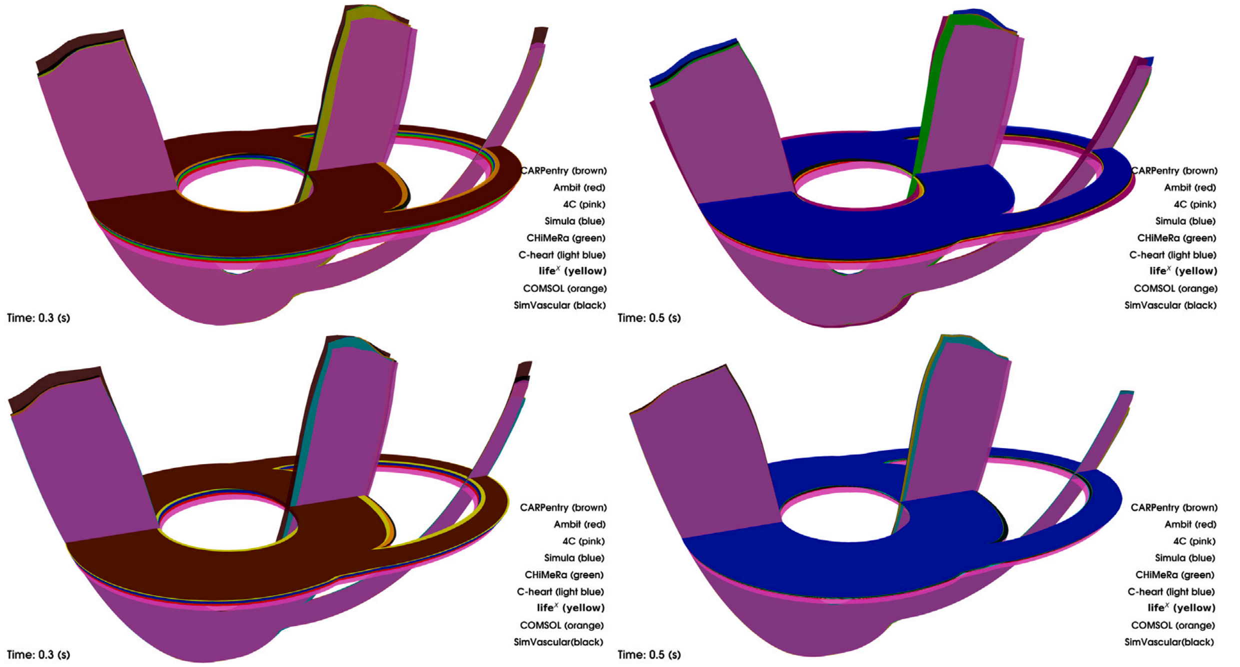

Fig. 14. Visual overlapping of each team solution using two-chamber and short-axis views, at two different time instants $t = 0.3$ [s] (left column) and $t = 0.5$ [s] (right column) in the coarse mesh Ω_{h_1} (top row) and fine mesh Ω_{h_2} (bottom row). (For interpretation of the references to color in this figure legend, the reader is referred to the web version of this article.)

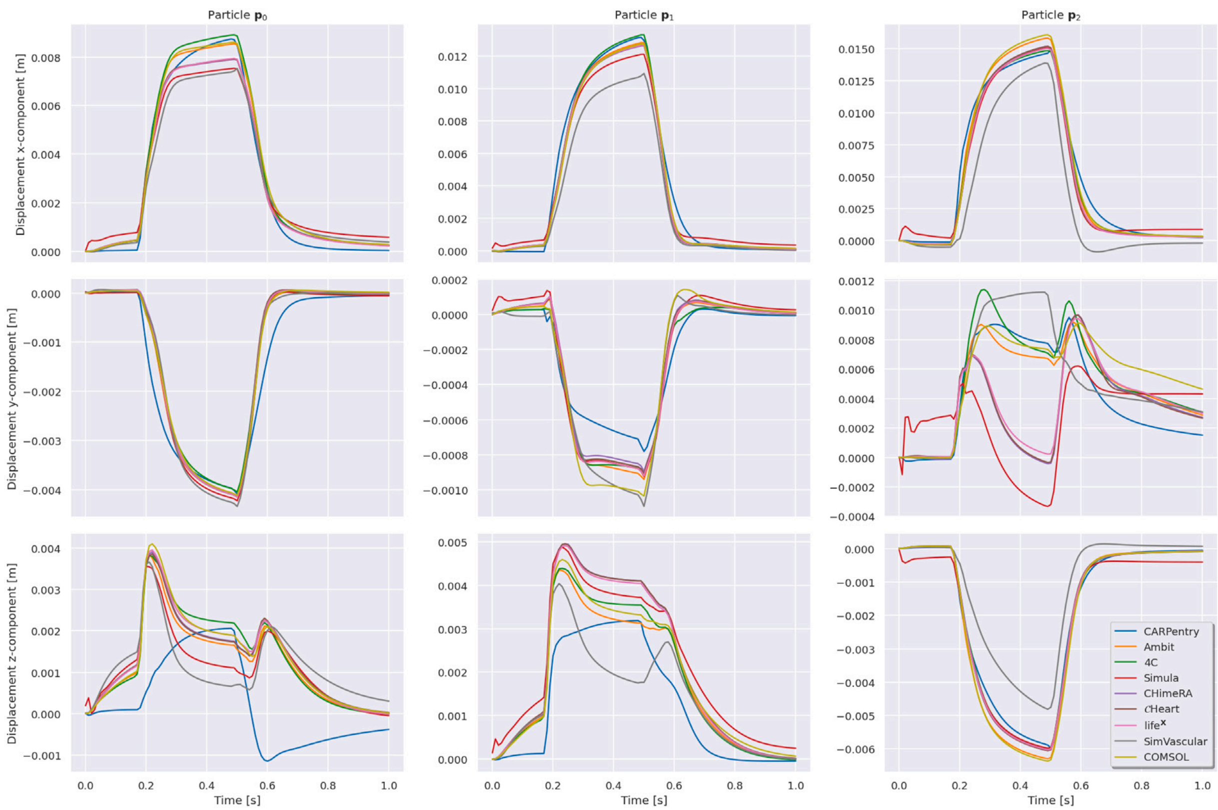

Fig. 15. Comparison per component of displacement $\mathbf{u}_h(\mathbf{p}_0)$ (left), $\mathbf{u}_h(\mathbf{p}_1)$ (center) and $\mathbf{u}_h(\mathbf{p}_2)$ (right) in the coarse mesh Ω_{h_1}. (For interpretation of the references to color in this figure legend, the reader is referred to the web version of this article.)

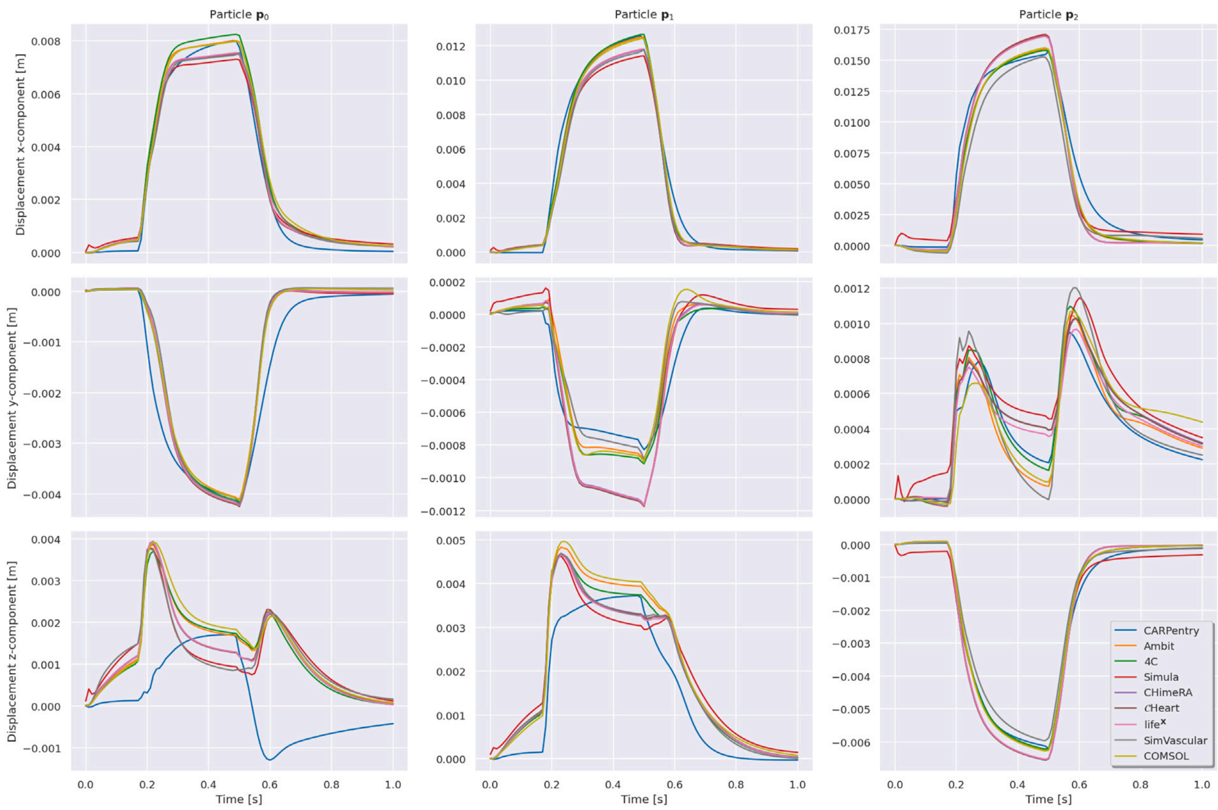

Fig. 16. Comparison per component of displacement $\mathbf{u}_h(\mathbf{p}_0)$ (left), $\mathbf{u}_h(\mathbf{p}_1)$ (center) and $\mathbf{u}_h(\mathbf{p}_2)$ (right) in the fine mesh Ω_{h_2}. (For interpretation of the references to color in this figure legend, the reader is referred to the web version of this article.)

study represents a significantly increased complexity compared with previous benchmarks in the field, and the inclusion of a more realistic geometry is left for a potential follow-up.

We restricted ourselves to the study of the constitutive model in [18], which is the most commonly used one in continuum-based, organ-scale simulations. In any case, apart from the newest viscoelastic model [71], we are not aware of important more recent developments in this field. Therefore, we believe our choice remains highly relevant due to the widespread use of the presented model. Providing benchmarks for other models, such as the ones reviewed recently in [72,73] is out of the scope of the present study.

Another limitation of this study consists in that the variability of the output to all model parameters (such that representing viscoelasticity and (in)compressibility) was not studied, though those effects where included in the model.

Though some insights for mesh sensitivity are given in Benchmark 2, this aspect was not fully explored in this article, and we consider relevant for future benchmarking efforts, together with reporting more quantities such as strains and stresses, which are often more sensitive to the discretization methods.

9. Conclusion

Consensus in simulation results is an important task, as several discretization parameters need to be selected. In this software benchmark for cardiac elastodynamics, a set of physiological test cases is proposed, comprising two different geometries. The methodology for assessment of results is based on a non-blinded calibration step and consecutive blinded steps. Nine research teams within the domain of cardiac mechanics participated in this benchmark. The benchmarks are structured as a series of steps with progressively increasing complexity, offering a step-by-step approach for verifying newly developed code. In the case of the monoventricular domain, which includes analytical fiber definition, consensus of solutions is observed in all displacement directions when changing the material parameters. Notably, different numerical methods and software implementations produced comparable results, with agreement between all participating teams. For the biventricular domain, an idealized geometry is introduced, with fibers based on the state-of-the-art in cardiac mechanics. Furthermore, tuned parameters for a physiological contraction are introduced, generalizing the previous monoventricular benchmark. The results for the biventricular model become more subject to differences arising from the incompressibility handling and space discretization as well as the fiber discretization. In this more challenging case, a few groups produced consistently comparable results (qualitatively and quantitatively), though using fully

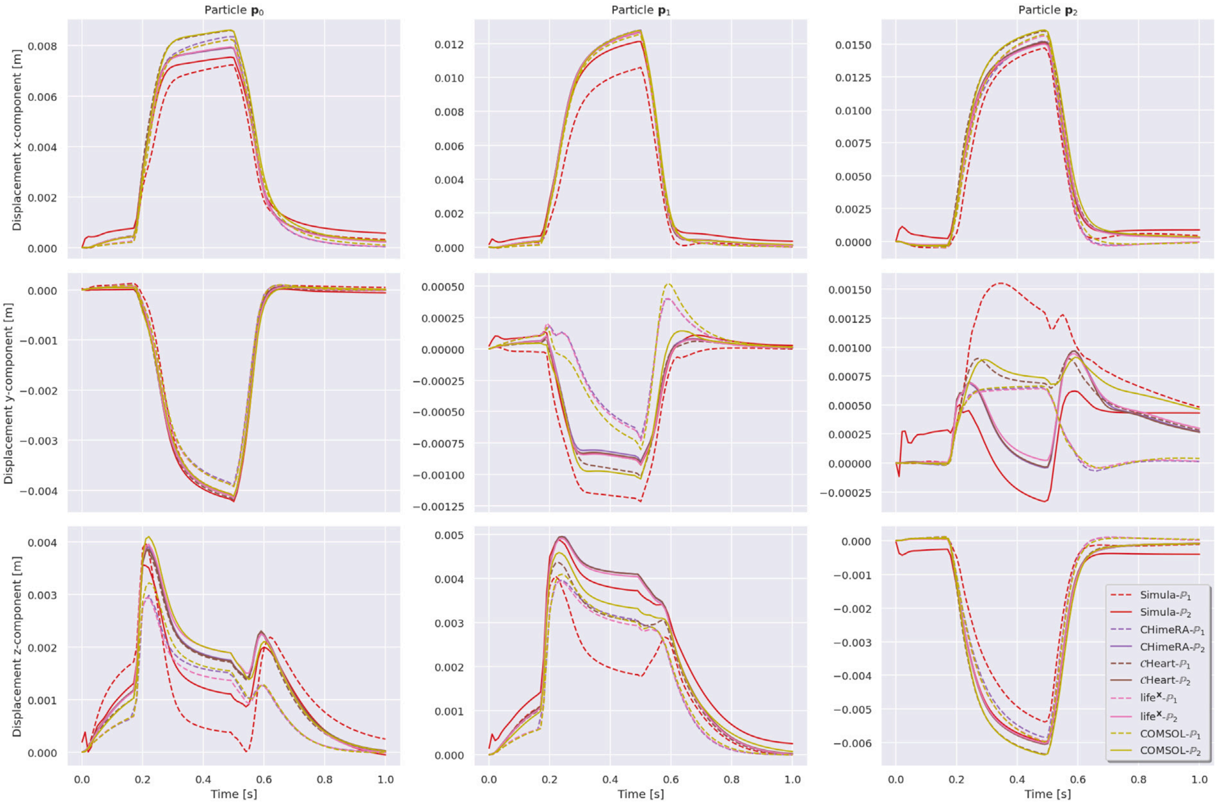

Fig. 17. Comparison per component of displacement $\mathbf{u}_h(\mathbf{p}_0)$ (left), $\mathbf{u}_h(\mathbf{p}_1)$ (center) and $\mathbf{u}_h(\mathbf{p}_2)$ (right) in the coarse mesh Ω_{h_1}. In dashed lines the $\mathbb{P}_1$ solutions and in full lines the $\mathbb{P}_2$ solutions. (For interpretation of the references to color in this figure legend, the reader is referred to the web version of this article.)

different software platform and libraries. However, it is important to note that since the test cases were deliberately chosen to be realistic and complex, it makes it difficult to determine the "reference" solutions. Nevertheless, overall the results will still serve as a range of values for valuable guidance to future authors and solver developers.

CRediT authorship contribution statement

Reidmen Aróstica: Writing – review & editing, Writing – original draft, Visualization, Validation, Software, Project administration, Methodology, Investigation, Data curation, Conceptualization. **David Nolte:** Writing – review & editing, Validation, Software. **Aaron Brown:** Writing – review & editing, Software. **Amadeus Gebauer:** Writing – review & editing, Software, Investigation. **Elias Karabelas:** Writing – review & editing, Software. **Javiera Jilberto:** Writing – review & editing, Software, Investigation. **Matteo Salvador:** Writing – review & editing, Software, Investigation. **Michele Bucelli:** Writing – review & editing, Software, Investigation. **Roberto Piersanti:** Writing – review & editing, Software, Investigation. **Kasra Osouli:** Writing – review & editing, Software, Investigation. **Christoph Augustin:** Writing – review & editing, Software, Investigation. **Henrik Finsberg:** Writing – review & editing, Software, Investigation. **Lei Shi:** Writing – review & editing, Software, Investigation. **Marc Hirschvogel:** Writing – review & editing, Software, Investigation. **Martin Pfaller:** Writing – review & editing, Software, Conceptualization. **Pasquale Claudio Africa:** Writing – review & editing, Software, Investigation. **Matthias Gsell:** Writing – review & editing, Software, Investigation. **Alison Marsden:** Supervision. **David Nordsletten:** Writing – review & editing, Supervision, Software. **Francesco Regazzoni:** Writing – review & editing, Software. **Gernot Plank:** Writing – review & editing, Software. **Joakim Sundnes:** Writing – review & editing, Software, Investigation. **Luca Dede':** Writing – review & editing, Supervision, Software, Investigation, Conceptualization. **Mathias Peirlinck:** Writing – review & editing, Software, Investigation, Conceptualization. **Vijay Vedula:** Writing – review & editing, Supervision, Software, Investigation, Conceptualization. **Wolfgang Wall:** Supervision. **Cristóbal Bertoglio:** Writing – review & editing, Supervision, Project administration, Methodology, Funding acquisition, Conceptualization.

Declaration of competing interest

The authors declare the following financial interests/personal relationships which may be considered as potential competing interests: Cristobal Bertoglio reports administrative support and article publishing charges were provided by University of Groningen. If there are other authors, they declare that they have no known competing financial interests or personal relationships that could have appeared to influence the work reported in this paper.

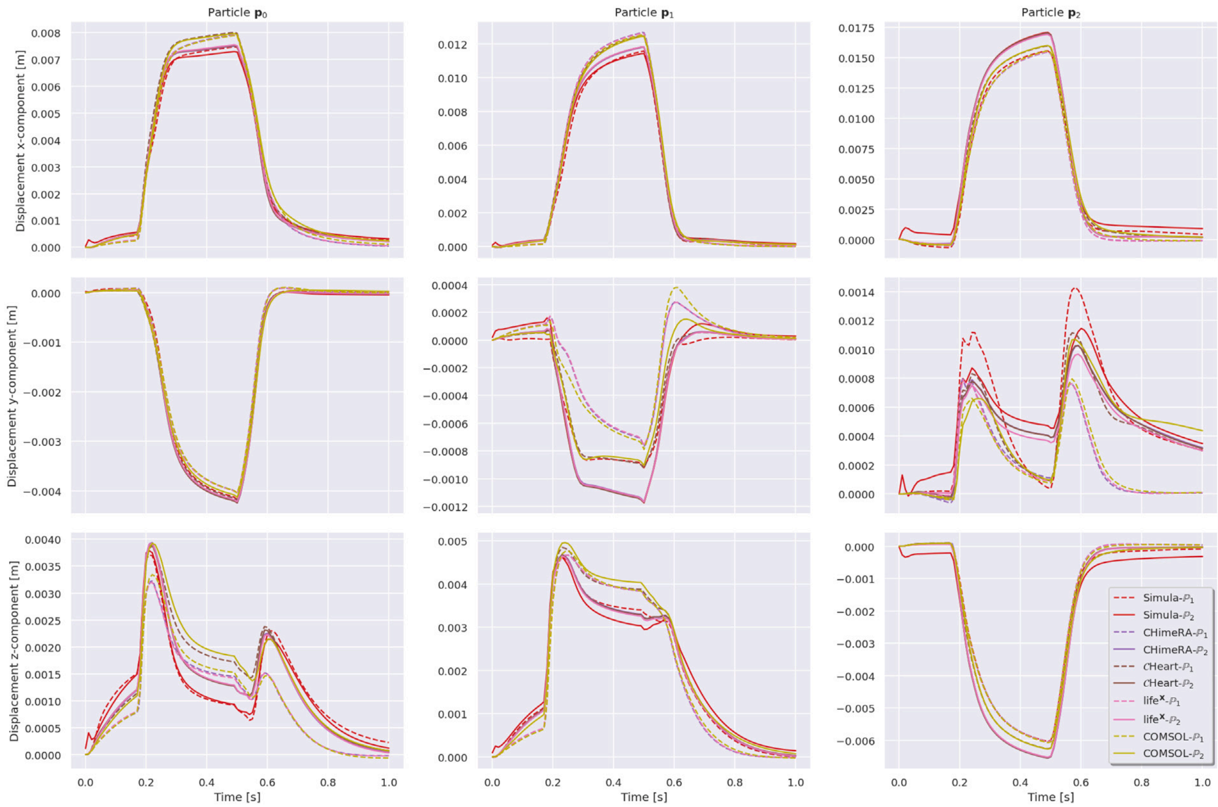

Fig. 18. Comparison per component of displacement $\mathbf{u}_h(\mathbf{p}_0)$ (left), $\mathbf{u}_h(\mathbf{p}_1)$ (center) and $\mathbf{u}_h(\mathbf{p}_2)$ (right) in the fine mesh Ω_{h_2}. In dashed lines the $\mathbb{P}_1$ solutions and in full lines the $\mathbb{P}_2$ solutions. (For interpretation of the references to color in this figure legend, the reader is referred to the web version of this article.)

Acknowledgments

R.A., D.N. and C.B. acknowledge the funding from the European Research Council (ERC) under the European Union's Horizon 2020 research and innovation programme (grant agreement No 852544 - CardioZoom).

H.F. and J.S. benefited from the Experimental Infrastructure for Exploration of Exascale Computing (eX3), which is financially supported by the Research Council of Norway under contract 270053.

R.P., M.B. and L.D. have received support from the project PRIN2022, MUR, Italy, 2023–2025, 202232A8AN "Computational modeling of the heart: from efficient numerical solvers to cardiac digital twins". R.P. also has received support from the INdAM, Italy GNCS project CUP E53C23001670001.

F.R. has received support from the project PRIN2022, MUR, Italy, 2023–2025, P2022N5ZNP "SIDDMs: shape-informed data-driven models for parametrized PDEs, with application to computational cardiology".

R.P., M.B., F.R. and L.D. acknowledge the "Dipartimento di Eccellenza 2023-2027", MUR, Italy, Dipartimento di Matematica, Politecnico di Milano, Italy.

P.C.A. acknowledges the consortium iNEST (Interconnected North-East Innovation Ecosystem), Piano Nazionale di Ripresa e Resilienza (PNRR), Italy – Missione 4 Componente 2, Investimento 1.5 – D.D. 1058 23/06/2022, ECS00000043, supported by the European Union's NextGenerationEU program.

R.P., M.B., F.R., P.C.A. and L.D. acknowledge their membership to INdAM GNCS - Gruppo Nazionale per il Calcolo Scientifico (National Group for Scientific Computing, Italy).

M.P. acknowledges support through the NWO Veni Talent Award, Italy 20058 and the European Union's Horizon Europe research and innovation programme under grant agreement No 101136728 (VITAL).

C.A. acknowledges funding by the Austrian Science Fund (FWF), grant DOIs 10.55776/P37063 and 10.55776/I4652. For open access purposes, the author has applied a CC BY public copyright license to any author-accepted manuscript version arising from this submission.

Appendix. Fiber convention

The most appropriate modeling choice for the fiber, sheet, and normal directions in the ventricular region remains an active area of debate within the community of cardiac mechanics. Variability in histological studies and computational methods to extract principal tissue directions exacerbate this discussion [20,21,34,74–76]. Whereas the transmural evolution of the myocardial fiber direction across the transmural wall seems to be well accepted, two main modeling approaches can be distinguished with respect to the assigned sheet and normal directions in computational ventricle models. Following the works in [18,20], various groups take the sheet direction ($\mathbf{s}$) to be oriented along the transmural direction and the normal direction ($\mathbf{n}$) to be orthogonal to both fiber and sheet directions [21,74,75,77,78]. Following the works in [6,7], other groups assume the normal direction ($\mathbf{n}$) to be oriented along the transmural direction and the sheet direction ($\mathbf{s}$) to be orthogonal to both fiber and normal directions. With proper tuning of the constitutive parameters, both approaches can lead to realistic deformation profiles during diastolic loading and systolic contraction. Given our choice to use tuned constitutive parameters from a group using the second convention, we followed their myocardial architecture convention for our monoventricular benchmark cases. In reality, sheet and normal vector fields can be considered to have transmural radial-longitudinal angle variations [34,76]. As such, both conventions provide a simplified but relevant approach towards simulating cardiac mechanics starting from the end-systolic and end-diastolic configuration, respectively.

Data availability

The input data and simulation results are publicly available in `Zenodo`. Some of the computational codes are also openly available: `CARPentry`, `Ambit`, `Simula's`, `SimVascular`, `life`^{x} .

References

[1] Andrew E. Anderson, Benjamin J. Ellis, Jeffrey A. Weiss, Verification, validation and sensitivity studies in computational biomechanics, Comput. Methods Biomech. Biomed. Eng. 10 (3) (2007) 171–184.

[2] Sander Land, Viatcheslav Gurev, Sander Arens, Christoph M. Augustin, Lukas Baron, Robert Blake, Chris Bradley, Sebastian Castro, Andrew Crozier, Marco Favino, Thomas E. Fastl, Thomas Fritz, Hao Gao, Alessio Gizzi, Boyce E. Griffith, Daniel E. Hurtado, Rolf Krause, Xiaoyu Luo, Martyn P. Nash, Simone Pezzuto, Gernot Plank, Simone Rossi, Daniel Ruprecht, Gunnar Seemann, Nicolas P. Smith, Joakim Sundnes, J. Jeremy Rice, Natalia Trayanova, Dafang Wang, Zhinuo Jenny Wang, Steven A. Niederer, Verification of cardiac mechanics software: benchmark problems and solutions for testing active and passive material behaviour, Proc. R. Soc. A 471 (2184) (2015) 20150641, http://dx.doi.org/10.1098/rspa.2015.0641.

[3] Katherine R. Saul, Xiao Hu, Craig M. Goehler, Meghan E. Vidt, Melissa Daly, Anca Velisar, Wendy M. Murray, Benchmarking of dynamic simulation predictions in two software platforms using an upper limb musculoskeletal model, Comput. Methods Biomech. Biomed. Eng. 18 (13) (2015) 1445–1458.

[4] Christoph Oefner, Sven Herrmann, Maeruan Kebbach, Hans-E Lange, Daniel Kluess, Matthias Woiczinski, Reporting checklist for verification and validation of finite element analysis in orthopedic and trauma biomechanics, Med. Eng. Phys. 92 (2021) 25–32.

[5] Vijay Vedula, Stefania Fortini, Jung-Hee Seo, Giorgio Querzoli, Rajat Mittal, Computational modeling and validation of intraventricular flow in a simple model of the left ventricle, Theor. Comput. Fluid Dyn. 28 (6) (2014) 589–604, http://dx.doi.org/10.1007/s00162-014-0335-4.

[6] Marc Hirschvogel, Marina Bassilious, Lasse Jagschies, Stephen M. Wildhirt, Michael W. Gee, A monolithic 3D-0d coupled closed-loop model of the heart and the vascular system: Experiment-based parameter estimation for patient-specific cardiac mechanics, Int. J. Numer. Methods Biomed. Eng. 33 (8) (2017) e2842, http://dx.doi.org/10.1002/cnm.2842.

[7] Martin R. Pfaller, Julia M. Hörmann, Martina Weigl, Andreas Nagler, Radomir Chabiniok, Cristóbal Bertoglio, Wolfgang A. Wall, The importance of the pericardium for cardiac biomechanics: from physiology to computational modeling, Biomech. Model. Mechanobiol. 18 (2) (2018) 503–529, http://dx.doi.org/10.1007/s10237-018-1098-4.

[8] Alfonso Santiago, Jazmín Aguado-Sierra, Miguel Zavala-Aké, Ruben Doste-Beltran, Samuel Gómez, Ruth Arís, Juan C. Cajas, Eva Casoni, Mariano Vázquez, Fully coupled fluid-electro-mechanical model of the human heart for supercomputers, Int. J. Numer. Methods Biomed. Eng. 34 (12) (2018) http://dx.doi.org/10.1002/cnm.3140.

[9] Christoph M. Augustin, Matthias A.F. Gsell, Elias Karabelas, Erik Willemen, Frits W. Prinzen, Joost Lumens, Edward J. Vigmond, Gernot Plank, A computationally efficient physiologically comprehensive 3D–0D closed-loop model of the heart and circulation, Comput. Methods Appl. Mech. Engrg. 386 (2021) 114092, http://dx.doi.org/10.1016/j.cma.2021.114092.

[10] Tobias Gerach, Steffen Schuler, Jonathan Fröhlich, Laura Lindner, Ekaterina Kovacheva, Robin Moss, Eike Moritz Wülfers, Gunnar Seemann, Christian Wieners, Axel Loewe, Electro-mechanical whole-heart digital twins: A fully coupled multi-physics approach, Mathematics 9 (11) (2021) 1247, http://dx.doi.org/10.3390/math9111247.

[11] M. Peirlinck, F. Sahli Costabal, J. Yao, J.M. Guccione, S. Tripathy, Y. Wang, D. Ozturk, P. Segars, T.M. Morrison, S. Levine, E. Kuhl, Precision medicine in human heart modeling, Biomech. Model. Mechanobiol. 20 (3) (2021) 803–831, http://dx.doi.org/10.1007/s10237-021-01421-z.

[12] Michele Bucelli, Alberto Zingaro, Pasquale Claudio Africa, Ivan Fumagalli, Luca Dede', Alfio Quarteroni, A mathematical model that integrates cardiac electrophysiology, mechanics, and fluid dynamics: Application to the human left heart, Int. J. Numer. Methods Biomed. Eng. 39 (3) (2023) http://dx.doi.org/10.1002/cnm.3678.

[13] Marco Fedele, Roberto Piersanti, Francesco Regazzoni, Matteo Salvador, Pasquale Claudio Africa, Michele Bucelli, Alberto Zingaro, Luca Dede', Alfio Quarteroni, A comprehensive and biophysically detailed computational model of the whole human heart electromechanics, Comput. Methods Appl. Mech. Engrg. 410 (2023) 115983, http://dx.doi.org/10.1016/j.cma.2023.115983.

[14] Will Zhang, Javiera Jilberto, Gerhard Sommer, Michael S. Sacks, Gerhard A. Holzapfel, David A. Nordsletten, Simulating hyperelasticity and fractional viscoelasticity in the human heart, Comput. Methods Appl. Mech. Engrg. 411 (2023) 116048, http://dx.doi.org/10.1016/j.cma.2023.116048.

[15] Cesare Corrado, Jean-Frédéric Gerbeau, Philippe Moireau, Identification of weakly coupled multiphysics problems. Application to the inverse problem of electrocardiography, J. Comput. Phys. 283 (2015) 271–298, http://dx.doi.org/10.1016/j.jcp.2014.11.041.

[16] Radomir Chabiniok, Vicky Y. Wang, Myrianthi Hadjicharalambous, Liya Asner, Jack Lee, Maxime Sermesant, Ellen Kuhl, Alistair A. Young, Philippe Moireau, Martyn P. Nash, et al., Multiphysics and multiscale modelling, data–model fusion and integration of organ physiology in the clinic: ventricular cardiac mechanics, Interface Focus 6 (2) (2016) 20150083.

[17] Alexandre Imperiale, Dominique Chapelle, Philippe Moireau, Sequential data assimilation for mechanical systems with complex image data: application to tagged-MRI in cardiac mechanics, Adv. Model. Simul. Eng. Sci. 8 (1) (2021) http://dx.doi.org/10.1186/s40323-020-00179-w.

[18] Gerhard A. Holzapfel, Ray W. Ogden, Constitutive modelling of passive myocardium: a structurally based framework for material characterization, Phil. Trans. R. Soc. A 367 (1902) (2009) 3445–3475, http://dx.doi.org/10.1098/rsta.2009.0091.
[19] J. Bestel, F. Clément, M. Sorine, A biomechanical model of muscle contraction, in: Medical Image Computing and Computer-Assisted Intervention – MICCAI 2001, Springer Berlin Heidelberg, 2001, pp. 1159–1161, http://dx.doi.org/10.1007/3-540-45468-3_143.
[20] Gerhard Sommer, Andreas J. Schriefl, Michaela Andrä, Michael Sacherer, Christian Viertler, Heimo Wolinski, Gerhard A. Holzapfel, Biomechanical properties and microstructure of human ventricular myocardium, Acta Biomater. 24 (2015) 172–192, http://dx.doi.org/10.1016/j.actbio.2015.06.031.
[21] Osman Gültekin, Gerhard Sommer, Gerhard A. Holzapfel, An orthotropic viscoelastic model for the passive myocardium: continuum basis and numerical treatment, Comput. Methods Biomech. Biomed. Eng. 19 (15) (2016) 1647–1664, http://dx.doi.org/10.1080/10255842.2016.1176155.
[22] Mathias Peirlinck, Juan A. Hurtado, Manuel K. Rausch, Adrian Buganza Tepole, Ellen Kuhl, A universal material model subroutine for soft matter systems, 2024, http://dx.doi.org/10.48550/ARXIV.2404.13144.
[23] Julius M. Guccione, Kevin D. Costa, Andrew D. McCulloch, Finite element stress analysis of left ventricular mechanics in the beating dog heart, J. Biomech. 28 (10) (1995) 1167–1177, http://dx.doi.org/10.1016/0021-9290(94)00174-3.
[24] H.M. Wang, H. Gao, X.Y. Luo, C. Berry, B.E. Griffith, R.W. Ogden, T.J. Wang, Structure-based finite strain modelling of the human left ventricle in diastole, Int. J. Numer. Methods Biomed. Eng. 29 (1) (2012) 83–103, http://dx.doi.org/10.1002/cnm.2497.
[25] A. Palit, G.A. Turley, S.K. Bhudia, R. Wellings, M.A. Williams, Assigning myocardial fibre orientation to a computational biventricular human heart model, in: IFMBE Proceedings, Springer International Publishing, 2014, pp. 144–147, http://dx.doi.org/10.1007/978-3-319-02913-9_37.
[26] Arnab Palit, Sunil K. Bhudia, Theodoros N. Arvanitis, Glen A. Turley, Mark A. Williams, Computational modelling of left-ventricular diastolic mechanics: Effect of fibre orientation and right-ventricle topology, J. Biomech. 48 (4) (2015) 604–612, http://dx.doi.org/10.1016/j.jbiomech.2014.12.054.
[27] Arnab Palit, Pasquale Franciosa, Sunil K. Bhudia, Theodoros N. Arvanitis, Glen A. Turley, Mark A. Williams, Passive diastolic modelling of human ventricles: Effects of base movement and geometrical heterogeneity, J. Biomech. 52 (2017) 95–105, http://dx.doi.org/10.1016/j.jbiomech.2016.12.023.
[28] Debao Guan, Jiang Yao, Xiaoyu Luo, Hao Gao, Effect of myofibre architecture on ventricular pump function by using a neonatal porcine heart model: from DT-MRI to rule-based methods, R. Soc. Open Sci. 7 (4) (2020) 191655, http://dx.doi.org/10.1098/rsos.191655.
[29] Roberto Piersanti, Francesco Regazzoni, Matteo Salvador, Antonio F. Corno, Luca Dede', Christian Vergara, Alfio Quarteroni, 3D–0D closed-loop model for the simulation of cardiac biventricular electromechanics, Comput. Methods Appl. Mech. Eng. 391 (2022) 114607, http://dx.doi.org/10.1016/j.cma.2022.114607.
[30] Denisa Martonová, Mathias Peirlinck, Kevin Linka, Gerhard A. Holzapfel, Sigrid Leyendecker, Ellen Kuhl, Automated Model Discovery for Human Cardiac Tissue: Discovering the Best Model and Parameters, Cold Spring Harbor Laboratory, 2024, http://dx.doi.org/10.1101/2024.02.27.582427.
[31] P. Wriggers, C. Miehe, Contact constraints within coupled thermomechanical analysis—A finite element model, Comput. Methods Appl. Mech. Engrg. 113 (3–4) (1994) 301–319, http://dx.doi.org/10.1016/0045-7825(94)90051-5.
[32] Dominique Chapelle, Patrick Le Tallec, Philippe Moireau, Michel Sorine, Energy-preserving muscle tissue model: formulation and compatible discretizations, Int. J. Multiscale Comput. Eng. 10 (2) (2012).
[33] Christophe Geuzaine, Jean-Francois Remacle, Gmsh, 2020, URL http://http://gmsh.info/.
[34] Roberto Piersanti, Pasquale C. Africa, Marco Fedele, Christian Vergara, Luca Dedè, Antonio F. Corno, Alfio Quarteroni, Modeling cardiac muscle fibers in ventricular and atrial electrophysiology simulations, Comput. Methods Appl. Mech. Engrg. 373 (2021) 113468, http://dx.doi.org/10.1016/j.cma.2020.113468.
[35] D. Sanchez-Quintana, V. Garcia-Martinez, J.M. Hurle, Myocardial fiber architecture in the human heart, Cells Tissues Organs 138 (4) (1990) 352–358, http://dx.doi.org/10.1159/000146966.
[36] Patrick A. Helm, Hsiang-Jer Tseng, Laurent Younes, Elliot R. McVeigh, Raimond L. Winslow, Ex vivo 3D diffusion tensor imaging and quantification of cardiac laminar structure, Magn. Reson. Med. 54 (4) (2005) 850–859, http://dx.doi.org/10.1002/mrm.20622, URL https://onlinelibrary.wiley.com/doi/abs/10.1002/mrm.20622.
[37] Farhad Pashakhanloo, Daniel A. Herzka, Hiroshi Ashikaga, Susumu Mori, Neville Gai, David A. Bluemke, Natalia A. Trayanova, Elliot R. McVeigh, Myofiber architecture of the human atria as revealed by submillimeter diffusion tensor imaging, Circulation: Arrhythmia Electrophysiol. 9 (4) (2016) http://dx.doi.org/10.1161/circep.116.004133.
[38] Nicolas Toussaint, Christian T. Stoeck, Tobias Schaeffter, Sebastian Kozerke, Maxime Sermesant, Philip G. Batchelor, In vivo human cardiac fibre architecture estimation using shape-based diffusion tensor processing, Med. Image Anal. 17 (8) (2013) 1243–1255, http://dx.doi.org/10.1016/j.media.2013.02.008.
[39] J.D. Bayer, R.C. Blake, G. Plank, N.A. Trayanova, A novel rule-based algorithm for assigning myocardial fiber orientation to computational heart models, Ann. Biomed. Eng. 40 (10) (2012) 2243–2254, http://dx.doi.org/10.1007/s10439-012-0593-5.
[40] Debao Guan, Xin Zhuan, William Holmes, Xiaoyu Luo, Hao Gao, Modelling of fibre dispersion and its effects on cardiac mechanics from diastole to systole, J. Engrg. Math. 128 (1) (2021) http://dx.doi.org/10.1007/s10665-021-10102-w.
[41] Pasquale Claudio Africa, life^x: A flexible, high performance library for the numerical solution of complex finite element problems, SoftwareX 20 (2022) 101252, http://dx.doi.org/10.1016/j.softx.2022.101252.
[42] Pasquale Claudio Africa, Roberto Piersanti, Marco Fedele, Luca Dede', Alfio Quarteroni, Lifex-fiber: an open tool for myofibers generation in cardiac computational models, BMC Bioinformatics 24 (1) (2023) http://dx.doi.org/10.1186/s12859-023-05260-w.
[43] J. Chung, G.M. Hulbert, A time integration algorithm for structural dynamics with improved numerical dissipation: The generalized-α method, J. Appl. Mech. 60 (2) (1993) 371–375, http://dx.doi.org/10.1115/1.2900803.
[44] C. Kadapa, W.G. Dettmer, D. Perić, On the advantages of using the first-order generalised-alpha scheme for structural dynamic problems, Comput. Struct. 193 (2017) 226–238, http://dx.doi.org/10.1016/j.compstruc.2017.08.013.
[45] Martin S. Alnæs, Anders Logg, Kristian B. Ølgaard, Marie E. Rognes, Garth N. Wells, Unified form language, ACM Trans. Math. Softw. 40 (2) (2014) 1–37, http://dx.doi.org/10.1145/2566630.
[46] Matthew W. Scroggs, Igor A. Baratta, Chris N. Richardson, Garth N. Wells, Basix: a runtime finite element basis evaluation library, J. Open Source Softw. 7 (73) (2022) 3982, http://dx.doi.org/10.21105/joss.03982.
[47] Matthew W. Scroggs, Jørgen S. Dokken, Chris N. Richardson, Garth N. Wells, Construction of arbitrary order finite element degree-of-freedom maps on polygonal and polyhedral cell meshes, ACM Trans. Math. Softw. 48 (2) (2022) 1–23, http://dx.doi.org/10.1145/3524456.
[48] Anders Logg, Garth N. Wells, DOLFIN, ACM Trans. Math. Softw. 37 (2) (2010) 1–28, http://dx.doi.org/10.1145/1731022.1731030.
[49] Anders Logg, Kent-Andre Mardal, Garth Wells (Eds.), Automated Solution of Differential Eq. by the Finite Element Method, Springer Berlin Heidelberg, 2012, http://dx.doi.org/10.1007/978-3-642-23099-8.
[50] Martin Alnæs, Jan Blechta, Johan Hake, August Johansson, Benjamin Kehlet, Anders Logg, Chris Richardson, Johannes Ring, Marie E. Rognes, Garth N. Wells, The FEniCS project version 1.5, Arch. Numer. Softw. 3 (2015) Starting Point and Frequency. Year: 2013.
[51] P.R. Amestoy, A. Buttari, J.-Y. L'Excellent, T. Mary, Performance and Scalability of the Block Low-Rank Multifrontal Factorization on Multicore Architectures, ACM Trans. Math. Software 45 (2019) 2:1–2:26.
[52] Xiaoye S. Li, James W. Demmel, SuperLU_DIST: A scalable distributed-memory sparse direct solver for unsymmetric linear systems, ACM Trans. Math. Softw. 29 (2) (2003) 110–140.

[53] Satish Balay, Shrirang Abhyankar, Mark F. Adams, Steven Benson, Jed Brown, Peter Brune, Kris Buschelman, Emil Constantinescu, Lisandro Dalcin, Alp Dener, Victor Eijkhout, Jacob Faibussowitsch, William D. Gropp, Václav Hapla, Tobin Isaac, Pierre Jolivet, Dmitry Karpeev, Dinesh Kaushik, Matthew G. Knepley, Fande Kong, Scott Kruger, Dave A. May, Lois Curfman McInnes, Richard Tran Mills, Lawrence Mitchell, Todd Munson, Jose E. Roman, Karl Rupp, Patrick Sanan, Jason Sarich, Barry F. Smith, Stefano Zampini, Hong Zhang, Hong Zhang, Junchao Zhang, PETSc/TAO Users Manual, Tech. Rep. ANL-21/39 - Revision 3.20, Argonne National Laboratory, 2023, http://dx.doi.org/10.2172/2205494.

[54] The Trilinos Project Team, The Trilinos Project Website.

[55] Bruce Leasure, David J. Kuck, Sergei Gorlatch, Murray Cole, Gregory R. Watson, Alain Darte, David Padua, Utpal Banerjee, Olaf Schenk, Klaus Gärtner, David Padua, Howard Jay Siegel, Bobby Dalton Young, Roy H. Campbell, Ümit undefinedatalyürek, Cevdet Aykanat, Jasmin Ajanovic, Stefan Schmid, Roger Wattenhofer, E. N. Mootaz Elnozahy, Evan W. Speight, Jian Li, Ram Rajamony, Lixin Zhang, Baba Arimilli, David Padua, Michael Gerndt, Michael Gerndt, David Padua, Jack B. Dennis, Barry Smith, George Almasi, Alexandros Stamatakis, Davide Sangiorgi, Davide Sangiorgi, David Padua, John A. Gunnels, Jack Dongarra, Piotr Luszczek, Bernd Mohr, Rudolf Eigenmann, Paul Feautrier, Christian Lengauer, David Padua, Pradip Bose, Joseph F. JaJa, Anshul Gupta, Rocco De Nicola, David Padua, David Padua, David Padua, Roger S. Armen, Eric R. May, Michela Taufer, Al Geist, PARDISO, in: Encyclopedia of Parallel Computing, Springer US, 2011, pp. 1458–1464, http://dx.doi.org/10.1007/978-0-387-09766-4_90.

[56] Christoph M. Augustin, Aurel Neic, Manfred Liebmann, Anton J. Prassl, Steven A. Niederer, Gundolf Haase, Gernot Plank, Anatomically accurate high resolution modeling of human whole heart electromechanics: A strongly scalable algebraic multigrid solver method for nonlinear deformation, J. Comput. Phys. 305 (2016) 622–646, http://dx.doi.org/10.1016/j.jcp.2015.10.045.

[57] Elias Karabelas, Gundolf Haase, Gernot Plank, Christoph M. Augustin, Versatile stabilized finite element formulations for nearly and fully incompressible solid mechanics, Comput. Mech. 65 (1) (2019) 193–215, http://dx.doi.org/10.1007/s00466-019-01760-w.

[58] Youcef Saad, Martin H. Schultz, GMRES: A generalized minimal residual algorithm for solving nonsymmetric linear systems, SIAM J. Sci. Stat. Comput. 7 (3) (1986) 856–869, http://dx.doi.org/10.1137/0907058.

[59] Marc Hirschvogel, Ambit – a FEniCS-based cardiovascular multi-physics solver, J. Open Source Softw. 9 (93) (2024) 5744, http://dx.doi.org/10.21105/joss.05744.

[60] 4C, 4C: A comprehensive multi-physics simulation framework, 2024, https://www.4c-multiphysics.org.

[61] Henrik Finsberg, Joakim Sundnes, A software benchmark for cardiac elastodynamics, 2024, http://dx.doi.org/10.5281/zenodo.10875818, URL https://github.com/finsberg/cardiac_benchmark.

[62] J. Lee, A. Cookson, I. Roy, E. Kerfoot, L. Asner, G. Vigueras, T. Sochi, S. Deparis, C. Michler, N.P. Smith, D.A. Nordsletten, Multiphysics computational modeling in $\boldsymbol{C}-\mathbf{Heart}$, SIAM J. Sci. Comput. 38 (3) (2016) C150–C178, http://dx.doi.org/10.1137/15m1014097.

[63] COMSOL Multiphysics, Introduction to COMSOL Multiphysics®, vol. 9, COMSOL Multiphysics, Burlington, MA, 1998, p. 2018.

[64] Mathias Peirlinck, Kevin L. Sack, Pieter De Backer, Pedro Morais, Patrick Segers, Thomas Franz, Matthieu De Beule, Kinematic boundary conditions substantially impact in silico ventricular function, Int. J. Numer. Methods Biomed. Eng. 35 (1) (2018) http://dx.doi.org/10.1002/cnm.3151.

[65] Chi Zhu, Vijay Vedula, Dave Parker, Nathan Wilson, Shawn Shadden, Alison Marsden, svFSI: A multiphysics package for integrated cardiac modeling, J. Open Source Softw. 7 (78) (2022) 4118, http://dx.doi.org/10.21105/joss.04118.

[66] Aaron L. Brown, Matteo Salvador, Lei Shi, Martin R. Pfaller, Zinan Hu, Kaitlin E. Harold, Tzung Hsiai, Vijay Vedula, Alison L. Marsden, A modular framework for implicit 3D–0D coupling in cardiac mechanics, Comput. Methods Appl. Mech. Engrg. 421 (2024) 116764, http://dx.doi.org/10.1016/j.cma.2024.116764.

[67] Lei Shi, Ian Y. Chen, Hiroo Takayama, Vijay Vedula, An optimization framework to personalize passive cardiac mechanics, Comput. Methods Appl. Mech. Engrg. 432 (2024) 117401, http://dx.doi.org/10.1016/j.cma.2024.117401.

[68] Jairo Rodríguez-Padilla, Argyrios Petras, Julie Magat, Jason Bayer, Yann Bihan-Poudec, Dounia El Hamrani, Girish Ramlugun, Aurel Neic, Christoph M. Augustin, Fanny Vaillant, et al., Impact of intraventricular septal fiber orientation on cardiac electromechanical function, Am. J. Physiol.-Heart Circulatory Physiol. 322 (6) (2022) H936–H952.

[69] Ruben Doste, David Soto-Iglesias, Gabriel Bernardino, Alejandro Alcaine, Rafael Sebastian, Sophie Giffard-Roisin, Maxime Sermesant, Antonio Berruezo, Damian Sanchez-Quintana, Oscar Camara, A rule-based method to model myocardial fiber orientation in cardiac biventricular geometries with outflow tracts, Int. J. Numer. Methods Biomed. Eng. 35 (4) (2019) e3185.

[70] Caroline H. Roney, Rokas Bendikas, Farhad Pashakhanloo, Cesare Corrado, Edward J. Vigmond, Elliot R. McVeigh, Natalia A. Trayanova, Steven A. Niederer, Constructing a human atrial fibre atlas, Ann. Biomed. Eng. 49 (2021) 233–250.

[71] David Nordsletten, Adela Capilnasiu, Will Zhang, Anna Wittgenstein, Myrianthi Hadjicharalambous, Gerhard Sommer, Ralph Sinkus, Gerhard A. Holzapfel, A viscoelastic model for human myocardium, Acta Biomater. 135 (2021) 441–457.

[72] M. Kojic, Miljan Milosevic, Bogdan Milicevic, Vladimir Geroski, Vladimir Simic, D. Trifunovic, Goran Stankovic, Nenad Filipovic, Computational model for heart tissue with direct use of experimental constitutive relationships, J. Serbian Soc. Comput. Mech. 15 (1) (2021) 1–23.

[73] Denisa Martonová, Mathias Peirlinck, Kevin Linka, Gerhard A. Holzapfel, Sigrid Leyendecker, Ellen Kuhl, Automated model discovery for human cardiac tissue: Discovering the best model and parameters, Comput. Methods Appl. Mech. Engrg. 428 (2024) 117078.

[74] Valentina Carapella, Rafel Bordas, Pras Pathmanathan, Maelene Lohezic, Jurgen E. Schneider, Peter Kohl, Kevin Burrage, Vicente Grau, Quantitative study of the effect of tissue microstructure on contraction in a computational model of rat left ventricle, in: Vincenzo Lionetti (Ed.), PLoS One 9 (4) (2014) e92792, http://dx.doi.org/10.1371/journal.pone.0092792.

[75] Simone Rossi, Toni Lassila, Ricardo Ruiz-Baier, Adélia Sequeira, Alfio Quarteroni, Thermodynamically consistent orthotropic activation model capturing ventricular systolic wall thickening in cardiac electromechanics, Eur. J. Mech. A Solids 48 (2014) 129–142, http://dx.doi.org/10.1016/j.euromechsol.2013.10.009.

[76] David Holz, Denisa Martonová, Emely Schaller, Minh Tuan Duong, Muhannad Alkassar, Michael Weyand, Sigrid Leyendecker, Transmural fibre orientations based on Laplace–Dirichlet-rule-based-methods and their influence on human heart simulations, J. Biomech. 156 (2023) 111643, http://dx.doi.org/10.1016/j.jbiomech.2023.111643.

[77] Mathias Peirlinck, Matthieu De Beule, Patrick Segers, Nuno Rebelo, A modular inverse elastostatics approach to resolve the pressure-induced stress state for in vivo imaging based cardiovascular modeling, J. Mech. Behav. Biomed. Mater. 85 (2018) 124–133, http://dx.doi.org/10.1016/j.jmbbm.2018.05.032, URL https://www.sciencedirect.com/science/article/pii/S1751616118300602.

[78] Debao Guan, Faizan Ahmad, Peter Theobald, Shwe Soe, Xiaoyu Luo, Hao Gao, On the AIC-based model reduction for the general holzapfel–ogden myocardial constitutive law, Biomech. Model. Mechanobiol. 18 (4) (2019) 1213–1232, http://dx.doi.org/10.1007/s10237-019-01140-6.